Summertime Subtropical Stationary Waves in the Northern Hemisphere: Variability, Forcing Mechanisms, and Impacts on Tropical Cyclone Activity

CHUAN-CHIEH CHANG,[a] ZHUO WANG,[a] MINGFANG TING,[b] AND ZHAO MING[c]

[a] *University of Illinois at Urbana–Champaign, Urbana, Illinois*
[b] *Lamont-Doherty Earth Observatory, Columbia University, Palisades, New York*
[c] *National Oceanic and Atmospheric Administration/Geophysical Fluid Dynamics Laboratory, Princeton, New Jersey*

(Manuscript received 8 April 2022, in final form 29 September 2022)

ABSTRACT: The interannual variability of summertime subtropical stationary waves, the forcing mechanisms, and their connections to regional tropical cyclone (TC) variability are investigated in this study. Two indices are identified to characterize the interannual variability of subtropical stationary waves: the longitudinal displacement of the zonal wavenumber-1 component (WN1) and the intensity change of the zonal wavenumber-2 component (WN2). These two indices are strongly anticorrelated and offer simple metrics to depict the interannual variability of subtropical stationary waves. Furthermore, the longitudinal displacement of the WN1 is significantly correlated with the variability of TC activity over the North Pacific and North Atlantic, and its influences on regional TC activity can be explained by variations in vertical wind shear, tropospheric humidity, and the frequency of Rossby wave breaking. The subtropical stationary waves are strongly related to precipitation anomalies over different oceanic regions, implying the possible impacts of low-frequency climate modes. Semi-idealized experiments using the Community Earth System Model version 2 (CESM2) show that the longitude of the WN1 is strongly modulated by ENSO, as well as SST anomalies over the Atlantic main development region and the central North Pacific. Further diagnosis using a baroclinic stationary wave model demonstrates the dominant role of diabatic heating in driving the interannual variability of stationary waves and confirms the impacts of different air–sea coupled modes on subtropical stationary waves. Overall, subtropical stationary waves provide a unified framework to understand the impacts of various forcing agents, such as ENSO, the Atlantic meridional mode, and extratropical Rossby wave breaking, on TC activity over the North Atlantic and North Pacific.

KEYWORDS: Planetary waves; Stationary waves; Diabatic heating; Tropical cyclones; Climate variability

1. Introduction and objectives

Stationary waves are planetary-scale, zonally asymmetric circulations that are relatively stable on seasonal time scales (Nigam and DeWeaver 2003). In boreal summer, stationary waves with a baroclinic vertical structure are primarily found in the northern tropics and subtropics, with the largest amplitude between 15° and 45°N (Wills et al. 2019; Fig. 1b). Two lower-tropospheric anticyclones underneath the upper-level troughs are present in the North Pacific and North Atlantic oceanic basins, and they constitute the descending branches of the regional Hadley cells (Nigam and DeWeaver 2003). Over land, the strongest and most extensive baroclinic circulation is found over Asia, with a low-level cyclone centered over northern India and Pakistan and an upper-level anticyclone over the Tibetan Plateau (Fig. 1a). These features are integral parts of the Asian monsoon circulation and can be regarded as the rotational response to latent heating over the Indian and western Pacific monsoon regions (Gill 1980; Hoskins and Rodwell 1995; Ting 1994). The baroclinic structure of the atmospheric circulation is also visible over North America and is manifested by a thermal low over the Gulf of California (Johnson 2003) and a weak upper-level ridge, which can be linked to the North American monsoon (e.g., Adams and Comrie 1997; Siu and Bowman 2019).

Stationary waves play an important role in maintaining the zonally symmetric circulations through meridional transport of momentum and heat (Nigam and DeWeaver 2003). Additionally, hydrological heterogeneity across different regions in the world are primarily sustained by subtropical stationary waves through moisture advection (Nigam and DeWeaver 2003). For example, the zonally asymmetric winds in the lower troposphere associated with stationary eddies set up the strength and spatial extent of Asian monsoon precipitation (Molnar et al. 2010; Chen and Bordoni 2014), as well as the Atlantic–Pacific asymmetry in ocean freshwater forcing (Ferreira et al. 2018; Wills and Schneider 2015). Furthermore, intense and localized subsidence resulting from the interaction between a Rossby wave train and the midlatitude westerlies is responsible for the hot, dry summers over the Middle East, eastern Sahara, and Mediterranean (Rodwell and Hoskins 1996; Simpson et al. 2015). The linkage between stationary waves and extreme weathers, such as heat waves, has received increasing attention in recent years (e.g., Coumou et al. 2014; Petoukhov et al. 2013; Schubert et al. 2011; Teng et al. 2013, 2016; White et al. 2022; Wolf et al. 2018). In particular,

Denotes content that is immediately available upon publication as open access.

Supplemental information related to this paper is available at the Journals Online website: https://doi.org/10.1175/JCLI-D-22-0233.s1.

Corresponding author: Chuan-Chieh Chang, cchang3@illinois.edu

DOI: 10.1175/JCLI-D-22-0233.1

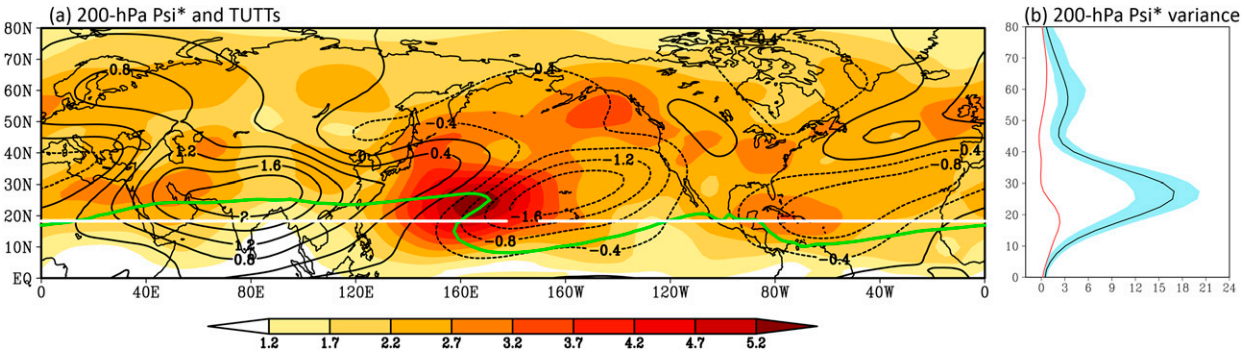

FIG. 1. (a) Long-term (1979–2018) mean 200-hPa Psi* (contours; 10^7 m^2 s^{-1}), interannual standard deviation of 200-hPa Psi* (shaded; 10^6 m^2 s^{-1}), 1 m s^{-1} climatological zonal geostrophic wind (U_g) contour (green line), and the reference latitude (white line) during July–October. Here the reference latitude is defined as the averaged latitude of climatological 1 m s^{-1} U_g contour, and the area where the circumglobal 1 m s^{-1} U_g contour extends southward of the reference latitude represents climatological Pacific and Atlantic TUTTs (see text in section 2a for details). (b) The long-term mean wave amplitude (10^{13} m^4 s^{-2}), 5th–95th percentile range of the seasonal-mean value (10^{13} m^4 s^{-2}), and the 40-yr trend [10^{13} m^4 s^{-2} (40 yr)$^{-1}$] are denoted by the black line, blue shading, and red line, respectively.

frequent occurrences of droughts and heavy rainfall events over the northern subtropical lands were found to have a close connection to the amplified subtropical stationary waves (Yuan et al. 2015).

Beyond the impacts on hydrological extremes and heat waves, very few studies have investigated the influences of hemispheric stationary waves on other hazardous weather systems, such as tropical cyclones (TCs; Wang et al. 2020). As one of the most severe storm systems on Earth, TCs induced more than $100 billion in property damages in the United States during 1980–2011 (Smith and Katz 2013). A better understanding of TC variability can help improve TC prediction and projection and is thus of social–economic significance. Previous studies mainly focused on how subtropical highs modulate TC tracks or genesis positions on a regional basis (e.g., Camp et al. 2019; Lenggenhager 2013; Mei et al. 2014; Wu et al. 2020). A recent study by Wang et al. (2020) suggested that summertime stationary waves in the Northern Hemisphere provides a unified framework that integrates the impacts of tropical and extratropical processes on TC variability. In particular, as part of the subtropical stationary waves (Fig. 1a), tropical upper-tropospheric troughs (TUTTs; Sadler 1967) are associated with variations in large-scale environmental conditions and Rossby wave breaking (RWB; e.g., Postel and Hitchman 1999; Waugh and Polvani 2000), and a strong anticorrelation exists between seasonal TC activity and TUTT extent (Wang et al. 2020). The maximum vorticity of TUTT is located approximately at 200 hPa, and the existence of an upper-level cold-core structure is necessary to maintain the thermal-wind balance (Fitzpatrick et al. 1995). In summertime, an east–west overturning circulation arises from the land–sea differential heating (Chen 2003; Magaña and Yanai 1991; Wallace and Hobbs 1977), and its descending branch dries the middle troposphere, leading to strong longwave radiative cooling over the subtropical North Pacific and North Atlantic, which is thought to be important in sustaining the regional cold-core structure of TUTTs (Geller and Avery 1978; Fitzpatrick et al. 1995; Knaff 1997).

Climatological stationary waves in the subtropics and at midlatitudes are maintained by rather different dynamics, which could be inferred from the different vertical structures (Chen 2005). These waves are characterized by a baroclinic structure in the subtropics, and by an equivalent barotropic structure at midlatitudes (White 1982). Using a linearized general circulation model (GCM) and a 15-yr simulation from a Geophysical Fluid Dynamics Laboratory (GFDL) GCM, Ting (1994) demonstrated that global diabatic heating plays the most important role in maintaining the climatological stationary waves in the northern subtropics and suggested that the flow structure over the Pacific Ocean and Asian continent is largely determined by heating over the Indian monsoon and western Pacific regions. The summertime extratropical stationary waves, in contrast, are largely forced by the stationary nonlinearity, and the nonlinear interaction between thermally driven flow and large orography is one of the important sources for the nonlinear effect (Chen and Trenberth 1988; Ting 1994; Ting et al. 2001).

Dynamical processes contributing to the interannual variability of extratropical stationary waves have been extensively investigated by previous studies (e.g., Coumou et al. 2014; Liu et al. 1998; Ma and Franzke 2021) since the midlatitude large-scale circulation anomalies are often associated with occurrences of extreme weather and hydrological events, for example, the floods during the summer of 1993 (Mo et al. 1995; Trenberth and Guillemot 1996). With a linear stationary wave model, Liu et al. (1998) concluded that the transient vorticity forcing has the predominant contribution to the anomalous extratropical wave train spanning from the North Pacific to the east coast of North America in the summer of 1993. Changes in transient vorticity fluxes have been also recognized to play a key role in maintaining the anomalous stationary waves linked to European heat waves in boreal summer (Ma and Franzke 2021; Schubert et al. 2011), and the nonlinear interaction between diabatic heating and topography was suggested to help amplify European blocking anticyclones (Ma and Franzke 2021). Interestingly, the extratropical

stationary wave anomalies induced by diabatic heating were found to be weak (Liu et al. 1998) or even opposite to the observed pattern (Ma and Franzke 2021).

Compared with extratropical stationary waves, the variability mechanisms of subtropical stationary waves in boreal summer have not been systematically investigated. The findings about extratropical stationary waves may not be directly applied to subtropical stationary waves since the basic wave dynamics changes from the Sverdrup regime in the tropics to the Rossby regime in the mid- to high latitudes (Chen 2005). In other words, the upper-level divergent circulation, which can be viewed as the driver of the rotational wind component (Sardeshmukh and Hoskins 1988), is primarily maintained by diabatic heating in the tropics and by both the sensible heat advection and diabatic heating in the mid- to high latitudes (Chen 2005). In this study, we will investigate the variability mechanisms of stationary waves, with a focus on the northern subtropics, using the reanalysis data, state-of-the-art GCMs, and a linearized simple stationary wave model. Specifically, we will address the following questions:

1) How do summertime stationary waves vary on the interannual time scales?
2) How is the variability of stationary waves related to TC activity over different basins?
3) What are the physical drivers for the interannual variability of subtropical stationary waves?

With the dynamical model spanning a spectrum of complexity, we will be able to identify the most influential forcing term and have a better understanding of how tropical and extratropical processes contribute to the variability of subtropical stationary waves. Impacts of different climate modes on stationary wave variability and TUTTs will also be explored. Compared to Wang et al. (2020), an observational study based on statistical analysis, this work seeks to bring us a deeper dynamical understanding of the physical processes and aims to provide new insight into the connections between atmospheric general circulation and regional TC variability. The rest of this paper is organized as follows. Section 2 describes the methodology, data, and experimental designs. The variability of stationary waves and the connection to regional TC activity are investigated in section 3. Physical mechanisms of the interannual stationary wave variability are discussed in section 4, followed by the summary and discussion in section 5.

2. Data, methodology, and experimental design

a. Data and methodology

We use monthly and 6-hourly data on isentropic and isobaric surfaces from the European Centre for Medium-Range Weather Forecasts (ECMWF) interim reanalysis (ERA-Interim, herein ERAI; Dee et al. 2011). The data are coarsened to a 2.5° grid spacing to facilitate computational efficiency. The 6-hourly potential vorticity (PV) field on the 350-K isentropic surface is used to detect anticyclonic Rossby wave breaking with an algorithm described in previous studies (Strong and Magnusdottir 2008; Zhang et al. 2016, 2017; Zhang and Wang 2018). In short, RWB is detected based on the overturning of PV contours, or the reversal of meridional PV gradient, and the algorithm records different features (e.g., time, centroid location, and area) of the equatorward high-PV tongues associated with wave breaking. If not specified otherwise, the monthly-mean data on pressure levels is used to examine the climatology and variations of the large-scale atmospheric environment. Monthly-mean SST and precipitation data are taken from the Extended Reconstructed Sea Surface Temperature, version 5 (ERSSTv5; Huang et al. 2017) and the Global Precipitation Climatology Project (GPCP; Adler et al. 2003), respectively. In addition, the 6-hourly TC track and intensity over the eastern Pacific and North Atlantic are taken from the HURDAT2 (Landsea and Franklin 2013), and TC information over the northwestern Pacific is from the Joint Typhoon Warning Center (JTWC) best track dataset. We focus on the TC peak season [July–October (JASO)] during 1979–2018.

The areal extent of the TUTTs is identified using the algorithm in Wang et al. (2020) with one modification. In Wang et al. (2020), the long-term mean geostrophic zonal wind (U_g) is first calculated with a fixed Coriolis parameter at 15°N using the climatological seasonal-mean (JASO) 200-hPa geopotential height, and the zonal-mean latitude of the 1 m s^{-1} U_g contour is defined as the reference latitude. The TUTT extent in each year is then estimated as the area where the seasonal mean circumglobal 1 m s^{-1} U_g contour extends equatorward of the reference latitude. Occasionally, the Pacific TUTT and the Atlantic TUTT are connected (see Fig. S2a in Wang et al. 2020). To divide two TUTTs, the original algorithm searches the longitude where a minimum latitudinal distance exists between the seasonal-mean 1 m s^{-1} U_g contour and the reference latitude. This longitude is referred as "dividing longitude." In the revised algorithm, the dividing longitude is determined by the position where the 200-hPa geopotential height averaged between 20° and 30°N reaches its maximum value between 80° and 120°W. This modification detects the central longitude of the North American monsoon anticyclone and enables the algorithm to split the two midocean troughs based on the large-scale flow characteristics.

b. CESM2 model setup

To better understand the role of different climate modes in modulating stationary waves and TUTTs, semi-idealized simulations forced by observed SST anomalies are performed using the CESM2 version 2.1.0 (Danabasoglu et al. 2020). Compared to CESM1, CESM2 has substantially reduced biases in large-scale circulation, tropical precipitation, and radiative flux (Danabasoglu et al. 2020; Simpson et al. 2020). The experiments are carried out with the "F2000climo" configuration of CESM2, which features the greenhouse gas emission and aerosol concentration in the year of 2000, and the Community Atmosphere Model version 6 (CAM6; Danabasoglu et al. 2020) is coupled with the Community Land Model version 5 (CLM5; Lawrence et al. 2019). Monthly model outputs are provided on a 0.94° × 1.25° (latitude × longitude) grid spacing.

A total of 220 ensemble members are integrated from 1 June to 1 November. The control experiment (CTRL) is forced by the climatological (1995–2005) monthly-varying SSTs and sea ice derived from the Hadley Centre sea ice and SST dataset version 1 (HadISST1; Rayner 2003). The model is first integrated for 5 months after initialization on 1 January, and 20 ensemble members are generated by introducing small round-off level differences in air temperature and specific humidity to the restart file on 1 June. Five sets of SST perturbation experiments, each consisting of 40 ensemble members (5×40), are carried out to investigate the impacts of changes in the following SST modes on large-scale circulations: Niño-3.4, the Pacific meridional mode (PMM), the Pacific decadal oscillation (PDO), the Atlantic multidecadal oscillation (AMO), and the Atlantic main development region (MDR) SST. Methodologies used to compute the time series of different SST indices are listed in appendix A. These climate modes have been demonstrated to have a close connection to the variability of TUTTs (Deng et al. 2018; Lu et al. 2017; Wang and Wu 2016; Wang et al. 2020). Time-independent SST anomalies, which correspond to ±1 standard deviation (STD) of various climate mode indices, are applied throughout the duration of the simulations (Fig. S1 in the online supplemental material). For each set of sensitivity experiment, the SST anomalies are added to (SST+) or subtracted from (SST−) the climatology (Fig. S1), and 20 ensembles are performed for the SST+ and SST− experiments. The linear response to different SST forcings is defined as the difference between the ensemble means of the SST+ and SST− experiments (SST+ minus SST−), scaled by a factor of 1/2. Simulations in June are discarded as the spinup stage for the sensitivity experiments, and model outputs are coarsened to a horizontal resolution of 2.5° × 2.5° for further analyses.

c. *Stationary wave model*

The time-dependent baroclinic stationary wave model (SWM) developed by Ting and Yu (1998) has been widely used in investigating the maintenance mechanisms of stationary waves from intraseasonal to multidecadal time scales (Jong et al. 2020; Ma and Franzke 2021; Simpson et al. 2016). The model solves the three-dimensional nonlinear primitive equations on the sigma (σ) coordinates and computes deviations from a zonal-mean basic state in response to zonally asymmetric prescribed forcings. The model is configured at a horizontal resolution of rhomboidal truncation R30 (roughly 2.25° × 3.75°) with 24 unevenly spaced vertical σ levels. Furthermore, meridional and zonal winds in the lowest four levels are subjected to Rayleigh friction with the strongest damping at the surface. To prevent baroclinic instability and reach a steady-state solution, an interior Rayleigh drag with a time scale of 15 days, a biharmonic diffusion with the coefficient of 10^{17} m^4 s^{-1} and a 15-day Newtonian cooling are imposed. The coefficients are the same as those used by Held et al. (2002) and Simpson et al. (2016). We run the model for 100 days, and the average from days 31 to 100 is shown.

The observed zonal-mean horizontal winds, air temperature, and surface pressure during July–October from 1979 to 2018 are used as the basic state for the SWM. The zonally asymmetric forcings, including diabatic heating and high-frequency momentum fluxes, are calculated using the 6-hourly data on the isobaric surfaces. Following Ling and Zhang (2013), diabatic heating is calculated as a residual from the three-dimensional thermodynamic equation [Eq. (B1)]. The aggregated effects of transient eddies cannot be explicitly simulated by the SWM and are included as an additional forcing term. Equations used to calculate the transient vorticity and divergence flux convergences are shown in appendix B [Eqs. (B2) and (B3)]. The zonal-mean basic state, diabatic heating, and transient momentum fluxes are first computed on the pressure levels and then linearly interpolated onto the model σ levels.

3. Interannual variability of subtropical stationary waves and its connection to regional TC activity

a. *Interannual variability of subtropical stationary waves*

The climatological TUTTs, spatial pattern of the long-term mean 200-hPa stationary waves, and their interannual variability are shown in Fig. 1a. The climatological stationary waves exhibit a global zonal wavenumber-2 pattern in the subtropics, and the variations of 200-hPa eddy streamfunction (Psi*) are relatively large on the western sides of the two mid-ocean troughs and the anticyclone above Tibet (Fig. 1a), with the strongest variability located between 150°E and 180°, consistent with a considerable east–west migration/extension of Pacific TUTT on the interannual time scale (Wang and Wu 2016). Following Yuan et al. (2015), the stationary wave amplitude is defined as the zonal variance of the 200-hPa Psi*. The long-term mean wave amplitude, the 5th–95th percentile range of the seasonal-mean value, and the 40-yr trend as a function of latitude are presented in Fig. 1b. The stationary wave reaches its maximum amplitude at around 25°N, and the strongest variability of wave amplitude occurs between 20° and 30°N (Fig. 1b). In agreement with previous studies (e.g., Yuan et al. 2015), the zonal variance of streamfunction exhibits an upward trend during the past 40 years, and the positive trend between 5° and 20°N is significant at 95% confidence level ($p < 0.05$) based on the Mann–Kendall test.

The Fourier decomposition provides a succinct approach to preserving the distinct features of stationary waves by a few selected harmonic components. Although not physically based, the Fourier decomposition is not localized and provides some advantage to depict the mean and variability of a large-scale field. When the longitudinal Fourier transform is applied to the 200-hPa Psi*, it is found that the wavenumber-1 component (WN1) makes the major contribution to the long-term mean Psi* variance (Fig. 2a) Also, its interannual variability is comparable to the wavenumber-2 component (WN2) between 20° and 30°N (Fig. 2b). Consistent with the earlier observational study by Krishnamurti (1971), these long waves account for most of the Psi* variance in the northern subtropics. We therefore focus on their year-to-year variability. Climatology and interannual variability of 200-hPa Psi* for zonal waves 1–2 are shown in Fig. 3. Before calculating the mean and standard deviation, the seasonal-mean 200-hPa Psi* is decomposed to different zonal wavenumbers in each year

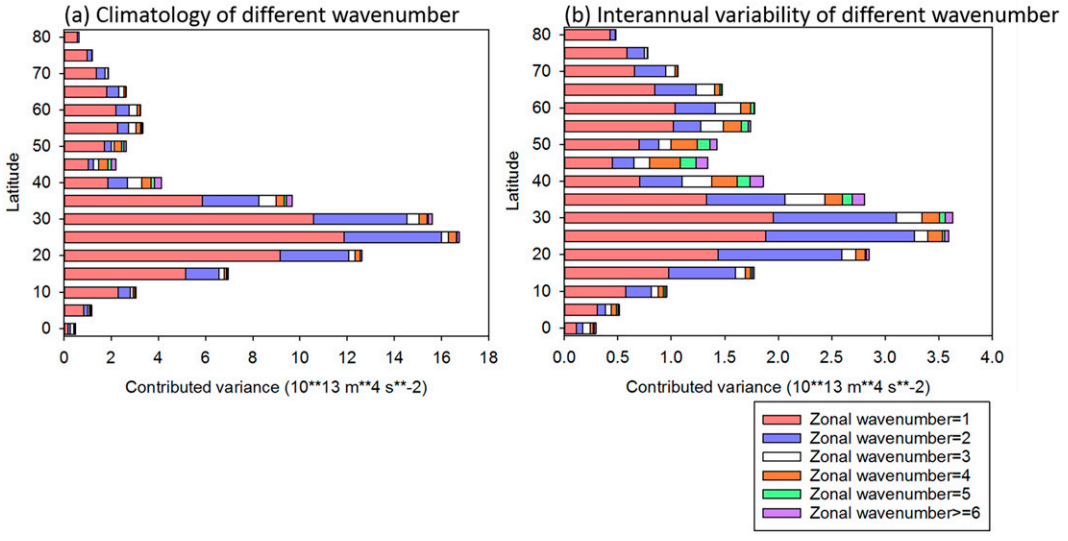

FIG. 2. (a) Long-term mean stationary wave amplitude (10^{13} m^4 s^{-2}) as a function of latitude and zonal wavenumber. (b) As in (a), but for interannual standard deviation of wave amplitude.

from 1979 to 2018. The maximum interannual variability of WN1 occurs between its two centers of action (Fig. 3a), while the maximum interannual variability of WN2 is nearly collocated with its centers of action (Fig. 3b). This suggests that the variability of WN1 is characterized by zonal displacement, whereas the variability of WN2 is dominated by intensity fluctuations.

To provide a quantitative measure of stationary wave variability, we define the intensity and position (i.e., latitude and longitude) indices of WN1 and WN2. Here, an intensity index is defined as the maximum value of Psi* of the corresponding wavenumber component over 0°–45°N, 0°–180°, and two position indices are defined as the longitude and latitude of the maximum Psi* (as denoted by the black dots in Fig. 3), respectively. Although WN1 and WN2 are not independent of each other (Table 1), such indices help to characterize the intensity and structural changes of stationary waves. The northward (southward) displacements of WN1 and WN2 are often accompanied by an eastward (westward) shift, as

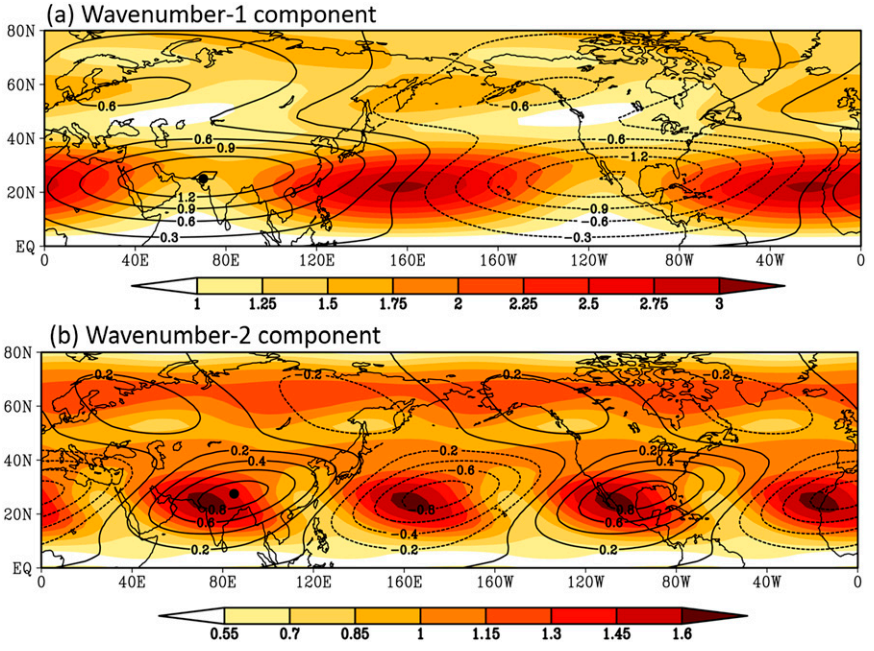

FIG. 3. Long-term mean (contours; 10^7 m^2 s^{-1}) and interannual variability (shaded; 10^6 m^2 s^{-1}) of 200-hPa Psi* for (a) WN1 and (b) WN2, respectively. Central positions of WN1 and WN2 are denoted by the black dots, respectively.

TABLE 1. Correlation of various wave metrics, including intensity, longitude, and latitude between WN1 and WN2. The bottom two lines show the correlations of different wave metrics with TUTT areal extents. Correlations exceeding the 95% confidence level are in bold and italic fonts.

	Wavenumber 1			Wavenumber 2		
	Intensity	Longitude	Latitude	Intensity	Longitude	Latitude
Wavenumber 1						
Intensity	1	−0.03	0.08	0.11	−0.03	0.15
Longitude	−0.03	1	***0.41***	***−0.77***	***0.57***	***0.45***
Latitude	0.08	***0.41***	1	−0.07	−0.01	−0.07
Wavenumber 2						
Intensity	0.11	***−0.77***	−0.07	1	***−0.53***	***−0.34***
Longitude	−0.03	***0.57***	−0.01	***−0.53***	1	***0.77***
Latitude	0.15	***0.45***	−0.07	***−0.34***	***0.77***	1
TUTT indices						
Pacific TUTT	0.09	***−0.71***	−0.25	***0.67***	***−0.36***	***−0.41***
Atlantic TUTT	0.03	***0.86***	0.13	***−0.74***	***0.47***	***0.5***

suggested by the positive correlations between their longitude and latitude indices. Also, the intensity of WN2 is negatively correlated to its longitude and latitude indices, suggesting that a stronger (weaker) WN2 is linked to a southwest (northeast) migration of its center. Furthermore, a strong negative correlation ($r = -0.77$) exists between WN1's longitude index and the intensity of WN2, consistent with the statement by Chen (2003) that WN1 is out of phase with the North American monsoon anticyclone, which is an integral part of the WN2. Meanwhile, the longitude index of WN1 and the intensity index of WN2 are significantly related to variations in TUTTs (Table 1). The main results based on the statistical analyses can be summarized as follows: an eastward shift of the WN1's center occurs in concert with a significantly weakened WN2 intensity. Such changes are associated with a weakened Pacific TUTT and a strengthened Atlantic TUTT. The opposite occurs when the WN1 shifts westward. In addition, the longitude index of WN1 shows a very strong correlation ($R = -0.91$) with the time series of the leading EOF mode (EOF1; Wang et al. 2020) of 200-hPa Psi*. The following analyses will thus focus on how changes in WN1's longitude relate to regional TC variability, and the physical driver responsible for the zonal displacement of WN1. On the other hand, we caution that a considerable amount of stationary wave variability is not captured by the longitude index of WN1 as it captures roughly 50% of the total variance in the areal change of Pacific TUTT. Also, about 40% of the variance in WN2 intensity cannot be explained by the zonal shift of WN1.

b. *Variability of subtropical stationary waves and TC activity*

The composites of TC track density are first constructed to illustrate the impacts of WN1's longitudinal position on regional TC activity. Based on the longitude index of WN1, we select 7 years when the position of WN1 is farthest east and 7 years when WN1's location is farthest west (see Fig. 4). These two groups are referred to as $WN1^+$ and $WN1^-$, respectively. When the WN1 displaces eastward, TC track density is reduced over the North Atlantic but enhanced over the northeastern Pacific (EPAC) and in the eastern portion of the western North Pacific (WNP; Fig. 4c). Meanwhile, the shift of WN1 is accompanied by significant changes in TUTTs (Figs. 4a,b) and RWB frequency (Figs. 4d,e). Relative to the $WN1^-$, $WN1^+$ is characterized by anomalously strong Atlantic TUTT and increasing occurrence of anticyclonic RWB over the subtropical North Atlantic and Gulf of Mexico (Figs. 4a,b,f), which facilitate tropical–extratropical mixing and equatorward intrusion of extratropical dry air (Postel and Hitchman 1999; Zhang et al. 2016, 2017; Wang et al. 2020). In contrast, the extent of the Pacific TUTT decreases for the $WN1^+$ relative to the $WN1^-$ (Figs. 4a,b), and RWBs happen less frequently over the subtropical central Pacific (Fig. 4f). Opposite changes of TUTTs (Figs. 4a,b) are consistent with the out-of-phase relationship observed by Wang et al. (2020) between two midocean troughs and could be explained by the impermeability of PV in the upper troposphere (Ortega et al. 2018). Variations of TC activity over the North Atlantic and the North Pacific can be partially attributed to changes in RWB frequency (Zhang et al. 2016, 2017; Wang et al. 2020), but TCs and TUTTs can both be modulated by other factors as will be discussed later.

The sharp contrast in TC track density prompts us to calculate the correlations of WN1's longitude with various TC indices (Table 2). Here, TC frequency (TCF) and hurricane frequency (HURR) are defined as the total number of TCs and hurricanes during July–October over a certain basin, respectively. A TC is categorized as a hurricane if the maximum 10-m wind speed exceeds 32 m s^{-1} during its lifetime. The accumulated cyclone energy (ACE; Bell et al. 2000) is calculated by summing the squares of the maximum 10-m wind speed (in knots) of every TC at 6-hourly intervals over a certain basin from July to October and then dividing it by 10 000. Strong negative correlations are found between the longitude index of WN1 and the Atlantic TC indices (TCF, HURR, and ACE), while the North Pacific TC indices, except the WNP TCF, show significant positive correlations with WN1's longitude (Table 2). It is possible that the east–west shift of WN1 affects TC

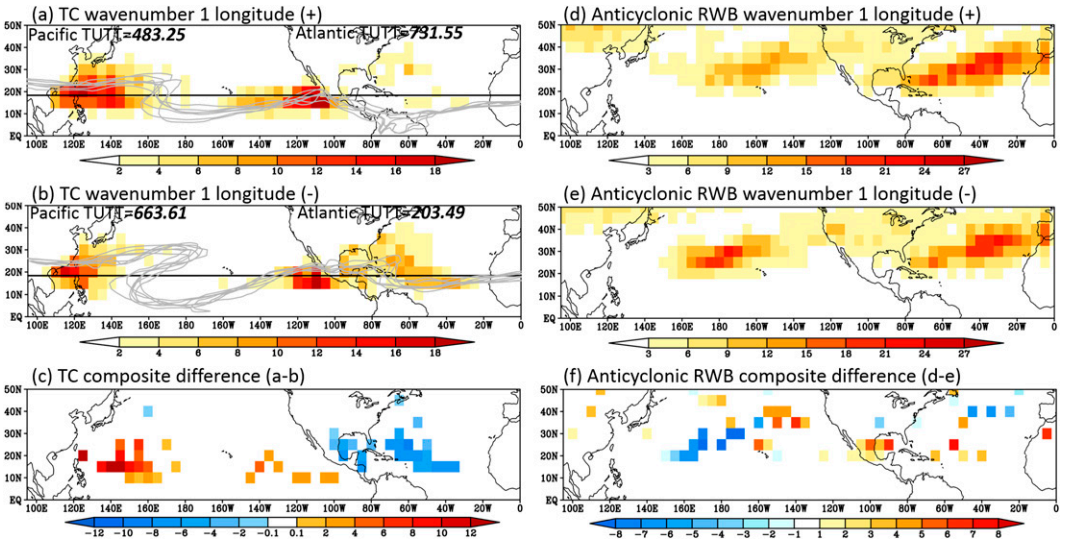

FIG. 4. Composite of seasonal-mean TC track density [counts per season (JASO) in a 5° × 5° grid cell] of (a) $WN1^+$ and (b) $WN1^-$, and (c) composite differences ($WN1^+$ minus $WN1^-$) of the TC track density. Composite of seasonal-mean RWB occurrence density [counts per season (JASO) in a 5° × 5° grid cell] of (d) $WN1^+$ and (e) $WN1^-$, and (f) composite differences ($WN1^+$ minus $WN1^-$) of the RWB occurrence density. In (a) and (b), reference latitude (black lines), averaged TUTT areal extents (10^4 km^2), and seasonal-mean 1 m s^{-1} U_g contours for individual years (gray lines) are shown for $WN1^+$ and $WN1^-$, respectively, and in (c) and (f) only differences significant at 90% confidence level are shown. The $WN1^+$ includes 1979, 1982, 1984, 1986, 1987, 1997, 2015, and years in the $WN1^-$ contain 1988, 1995, 1998, 1999, 2008, 2010, 2011.

genesis locations over the WNP (Wang and Wu 2016) but does not affect the basinwide TCF as discussed next in the context of large-scale circulation anomalies.

To understand the associated TC variability, it is instructive to examine the changes in the large-scale environmental conditions related to WN1. The total precipitable water (TPW) and vertical wind shear (VWS; defined as the magnitude of the vector wind difference between 200 and 850 hPa) anomalies corresponding to +1 STD of WN1's longitude index are shown in Fig. 5. When the WN1 component shifts eastward, VWS increases over the tropical North Atlantic but decreases over the eastern portion (90°–120°W) of the EPAC and in the central Pacific (Fig. 5a); negative TPW anomalies prevail over the tropical North Atlantic and along the coast of East Asia, but a broad region east of 140°E over the tropical–subtropical North Pacific is characterized by enhanced TPW (Fig. 5d). The regression patterns resemble those based on the TUTT indices (see Fig. 1 in Wang et al. 2020). The variations in environmental conditions are consistent with the suppressed TC activity over the North Atlantic and support TC genesis and intensification over the central and east Pacific (Fig. 4a). Over the WNP, the TPW and VWS anomalies suggest conducive conditions for TC development over the eastern WNP but a somewhat hostile environment over the subtropical western Pacific. This contributes to an eastward shift of TC genesis locations (Wang and Wu 2016) and increases the chance of TCs to intensify into typhoons but may not strongly modulate the basinwide TC frequency, which explains the significant correlation of WN1's longitude with ACE but a much weaker correlation with the TC frequency over this region.

As documented by mounting evidence (e.g., Bhardwaj et al. 2019; Camargo and Sobel 2005; Chan 1985; Elsner and Kara 1999; Gray 1984; Wu and Lau 1992), ENSO is known to affect TC activity over different basins in the Northern Hemisphere through modulations of various environmental factors (Camargo

TABLE 2. Numbers in the middle column indicate correlations of WN1's longitude index with various TC indices (listed at left); partial correlations between TC indices and WN1's longitude index, with the influences from ENSO removed, are shown in the right column. Values are shown for three basins, the North Atlantic (100°W–10°E), the northeastern Pacific (180°–85°W), and the northwestern Pacific (105°E–180°). Correlations exceeding the 95% confidence level are in bold italic font.

	Wavenumber-1 longitude	Wavenumber-1 longitude (remove Niño-3.4)
Atlantic TC indices		
TCF	***−0.65***	***−0.56***
HURR	***−0.63***	***−0.45***
ACE	***−0.54***	***−0.37***
East Pacific TC indices		
TCF	***0.61***	***0.39***
HURR	***0.5***	***0.34***
ACE	***0.53***	0.2
West Pacific TC indices		
TCF	0.25	0.14
Typhoon	***0.37***	0.08
ACE	***0.52***	−0.05

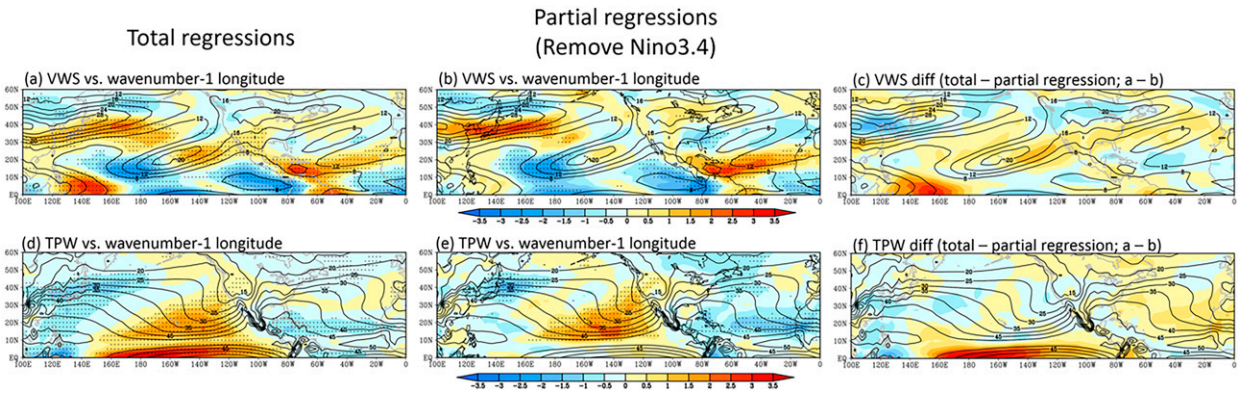

FIG. 5. (a) VWS and (d) TPW anomalies corresponding to +1 STD of WN1's longitude index. (b),(e) As in (a) and (d), but the influences from Niño-3.4 SST are removed using linear regression. The black contours show the 1979–2018 climatology, and black dots denote regions where the anomalies are significant at 95% confidence level. (c) Difference in VWS anomalies between (a) and (b) [(a) minus (b); total regression minus partial regression]. (f) As in (c), but for difference in TPW.

et al. 2007). It is natural to ask whether the stationary wave–TC relationship identified here simply reflect the impacts of ENSO. To address this question, we calculate partial correlations between WN1 longitude and the various TC indices, with the impact of Niño-3.4 SST removed using least squares linear regression (Table 2). In addition, partial linear regressions of VWS and TPW onto WN1 longitude are calculated using the same approach (Figs. 5b,e). After the removal of Niño-3.4 SST impact, WN1 longitude is still significantly correlated to TC variability over the North Atlantic, but its correlations with various TC indices become weaker over the EPAC and are insignificant over the WNP (Table 2). In addition, the differences between the partial linear regressions and total linear regressions are calculated (Figs. 5c,f). Such differences represent the impacts of ENSO on VWS and TWP via WN1, and they are the strongest over the tropical western and central Pacific, while the signals over the Atlantic are much weaker and even oppose to the partial regressions associated with WN1 (Figs. 5b,e). Overall, Fig. 5 suggests that ENSO is an important contributor to the link between stationary waves and TC activity, especially over the northwestern Pacific. However, the WN1–TC relationship cannot be completely attributed to ENSO, especially over the Atlantic and EPAC. Forcing factors for stationary wave variability other than ENSO will be also examined in the next section.

4. Underlying physical mechanisms responsible for interannual variability of subtropical stationary waves

a. Linkage to different climate modes and monsoon indices as revealed by observational data

Planetary-scale waves in the subtropics are largely driven by global diabatic heating (Ting 1994), or precipitation anomalies, which are closely related to tropical SST anomalies (Neelin and Held 1987). We therefore regress SST and precipitation onto the WN1 longitude and scale the regression coefficients such that they represent the anomalies associated with +1 STD of WN1's longitude (Figs. 6a,c). Variations in SST and precipitation are a combination of the positive phase of ENSO and PDO (Zhang et al. 1997) and the negative phase of AMO (Enfield et al. 2001; Fig. 6a). The significant negative SST anomalies over the North Atlantic MDR and subpolar gyre region, along with the weak but positive anomaly in the midlatitudes (Fig. 6a), are reminiscent of the tripole pattern identified by Czaja and Marshall (2001) and could be considered as the response of SST to a positive North Atlantic Oscillation (NAO) state in the preceding spring (Czaja and Marshall 2001; Czaja and Frankignoul 2002; Cassou et al. 2004). Over the Pacific, deviations of SST bear resemblance to the "mega ENSO" pattern (Mantua et al. 1997; Zhang et al. 1997; Wang et al. 2013). In particular, the positive PMM-like (Chiang and Vimont 2004) SST anomalies over the subtropical northeastern Pacific can propagate to the equatorial Pacific and lead to development of an El Niño event through the wind–evaporation feedback (Alexander et al. 2010). Precipitation anomalies over the tropical oceans are broadly consistent with changes in SST (Fig. 6b). Pronounced reductions of precipitation are observed over the tropical North Atlantic, Central America, and the Maritime Continent, while precipitation surplus is visible over the equatorial Pacific and tropical North Pacific (Fig. 6b) when the WN1 shifts eastward.

Significant precipitation anomalies not only are present over the tropical oceans, but also occur over different continental monsoon regions (Fig. 6c), indicating the impacts of summer monsoons on stationary waves. The possible role of monsoon heating in driving stationary wave variability is investigated by calculating the correlation coefficients of WN1 longitude with various monsoon indices (Table 3), including the Central American monsoon (Wang and Ding 2008), West African monsoon (Akinsanola and Zhou 2020), South Asian monsoon (Webster and Yang 1992), Maritime Continent monsoon (Xu and Guan 2017), and western North Pacific monsoon (Wang et al. 2001). The definitions of these monsoon indices are provided in appendix C. An eastward shift of WN1 is associated with significant weakening of most monsoon systems except the western North Pacific monsoon (Table 3). Further investigation reveals a strong connection of WN2 intensity with the South

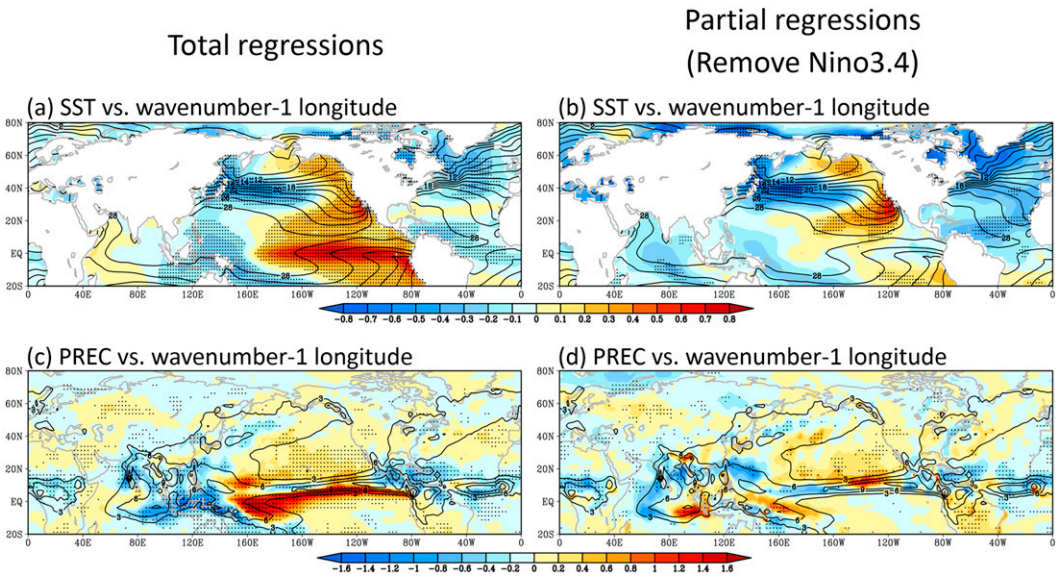

FIG. 6. (a) SST and (c) precipitation changes accompanying an increase of one STD in WN1's longitude. (b),(d) As in (a) and (c), but the influences from Niño-3.4 SST are removed using linear regression. The black contours show the 1979–2018 climatology, and the stippled area denotes regions where the anomalies are significant at 95% confidence level.

Asian monsoon (r = 0.74), Maritime Continent monsoon (r = 0.71), and North American monsoon (r = 0.54). Atmospheric response triggered by enhanced or weakened monsoon heating, in turn, can modify the characteristics of large-scale moisture transport and feedback to the monsoon rainfall. Consequently, the location and strength of subtropical planetary waves in the lower troposphere are coupled to changes in the regional precipitation (Li et al. 2011; Wang et al. 2001; Yuan et al. 2015).

TABLE 3. Numbers in the middle column indicate correlations of WN1's longitude index with various climate and monsoon indices (listed at left); partial correlations of WN1's longitude index with various climate and monsoon indices, with the influences from ENSO removed, are shown in the right column. Correlations exceeding the 95% confidence level are in bold italic font.

	Wavenumber-1 longitude	Wavenumber-1 longitude (remove Niño-3.4)
SST indices		
Niño-3.4	***0.79***	
PDO	***0.72***	***0.65***
PMM	***0.66***	***0.43***
MDR SST	***−0.44***	***−0.54***
AMO	***−0.68***	***−0.63***
Monsoon indices		
South Asian monsoon	***−0.75***	−0.21
Maritime Continent monsoon	***−0.62***	0.12
North American monsoon	***−0.58***	−0.13
West African monsoon	***−0.67***	−0.29
Western North Pacific monsoon	***0.3***	0.02

Although variability of stationary waves shows strong linkage to the strength of various regional monsoons, several studies suggested that summer monsoon precipitation could be strongly dictated by ENSO variability (Chang et al. 2000; Joly and Voldoire 2009; Webster and Yang 1992; Wang and Ding 2008; Xu and Guan 2017). The important role of ENSO is further supported by the weak and insignificant partial correlations between various monsoon indices and WN1's longitude when the influence of the ENSO is controlled (Table 3). Additionally, ENSO has a strong correlation with the longitude index of WN1 (r = 0.79). A straightforward way to understand how ENSO modulates subtropical stationary waves is through altering the Walker circulation and its associated divergent winds (Fig. S2). The above-normal SST east of the date line (Fig. 6a) shifts areas of enhanced convection eastward (Fig. S2) and establishes an upper-level Rossby wave source in the eastern part of equatorial Pacific (Sardeshmukh and Hoskins 1988), driving changes in rotational winds. Nevertheless, other SST indices, such as the PDO, PMM, AMO, and MDR SST, are also found to have significant correlations with the zonal displacement of WN1 (Table 3). This leads us to further explore the relative importance of ENSO and other air–sea coupled climate modes in driving the variability of subtropical stationary waves. The signal of Niño-3.4 SST is first removed from WN1's longitude index, global precipitation, and SST by linear regression, and then the linear regression coefficients at each grid point between the residual time series of precipitation/SST and the longitude index of WN1 are calculated (Figs. 6b,d). With the influences from ENSO removed, precipitation anomalies are largely diminished between 15°S and 15°N (Fig. 6d), consistent with the substantially weakened SST anomalies over the equatorial

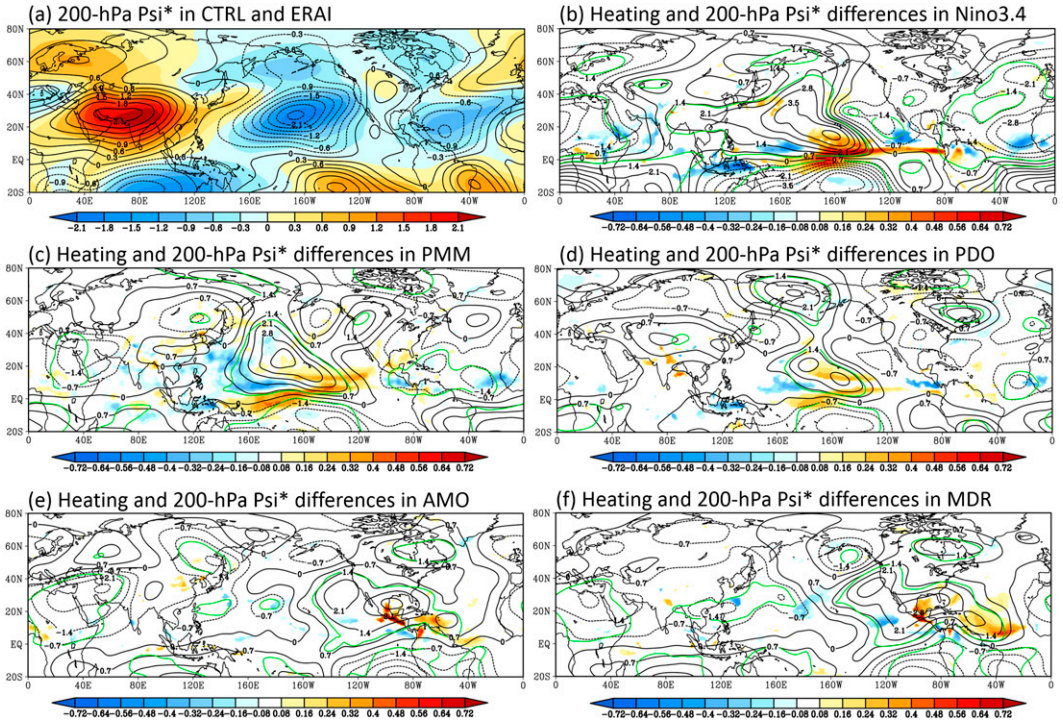

FIG. 7. (a) Climatological (1995–2005) 200-hPa Psi* from ERAI (shading; 10^7 m^2 s^{-1}) and ensemble-mean 200-hPa Psi* in CTRL experiment (contours; 10^7 m^2 s^{-1}). (b)–(f) Responses of 200-hPa Psi* (contours; 10^6 m^2 s^{-1}) and pressure-weighted column-averaged diabatic heating (K day^{-1}) associated with different SST forcings. Green contours depict 200-hPa Psi* differences exceeding the 95% confidence level, and only the diabatic heating differences significant at the 95% confidence level are shown.

Pacific and equatorial Atlantic (Fig. 6b). However, SST anomalies remain largely unchanged over the subtropical northeastern Pacific and are slightly enhanced over the North Atlantic (Fig. 6b), and significant changes in precipitation are still observed over the tropical and subtropical North Pacific and North Atlantic (Fig. 6d). The pattern of the residual SST and precipitation anomalies could be regarded as the footprint of the positive PMM (Chiang and Vimont 2004) and the negative Atlantic meridional mode (AMM; Nobre and Shukla 1996) in the preceding spring season. Furthermore, the PDO, PMM, AMO, and MDR SST indices are still significantly correlated to the longitude index of WN1 after the ENSO signals are removed (Table 3), suggesting the roles of various climate modes in driving the variability of subtropical stationary waves.

b. *Explore the relative impacts of different air–sea coupled modes using CESM2*

The observational analysis in the previous section helps reveal connections between the various climate modes and the zonal displacement of WN1, but it is challenging to determine the causality owing to the atmosphere–ocean coupling and the interaction between different climate modes. The different low-frequency climate modes discussed above are known to influence each other (e.g., Ham et al. 2013; Li et al. 2016). For example, warm SST anomalies in the tropical North Atlantic during the boreal spring can induce cooling over the subtropical northeastern Pacific and trigger a La Niña event in the following summer–fall seasons via a subtropical atmospheric teleconnection (Ham et al. 2013). To explore the causal direction and the relative impacts of different climate modes on stationary wave variability, semi-idealized CESM2 experiments are performed. Possible impacts related to interbasin interaction of different climate modes are ignored, and we just prescribe SST anomalies over a local basin (Fig. S1).

The stationary waves simulated by the CTRL are generally in good agreement with the ERAI reanalysis, but discrepancies are noticeable (Fig. 7a). Relative to the ERAI reanalysis, the simulated intensity of Pacific and Atlantic TUTTs is slightly stronger. Also, the central location of the monsoon anticyclone over Tibet shifts westward in CESM2 compared to the observed center (Fig. 7a). Responses of 200-hPa Psi* and diabatic heating to different SST forcings are shown in Figs. 7b–f. For the ENSO (Fig. 7b) experiment, there is enhanced diabatic heating over the equatorial Pacific between 120° and 180°W, but heating over the northern Indian Ocean and the western North Pacific is suppressed. In addition, significant negative heating anomalies over Central America, East Africa, and the Maritime Continent are consistent with the rainfall reductions observed over these regions during the warm ENSO episodes (Dai and Wigley 2000). It is worth pointing out that the tropospheric response in Fig. 7b is not

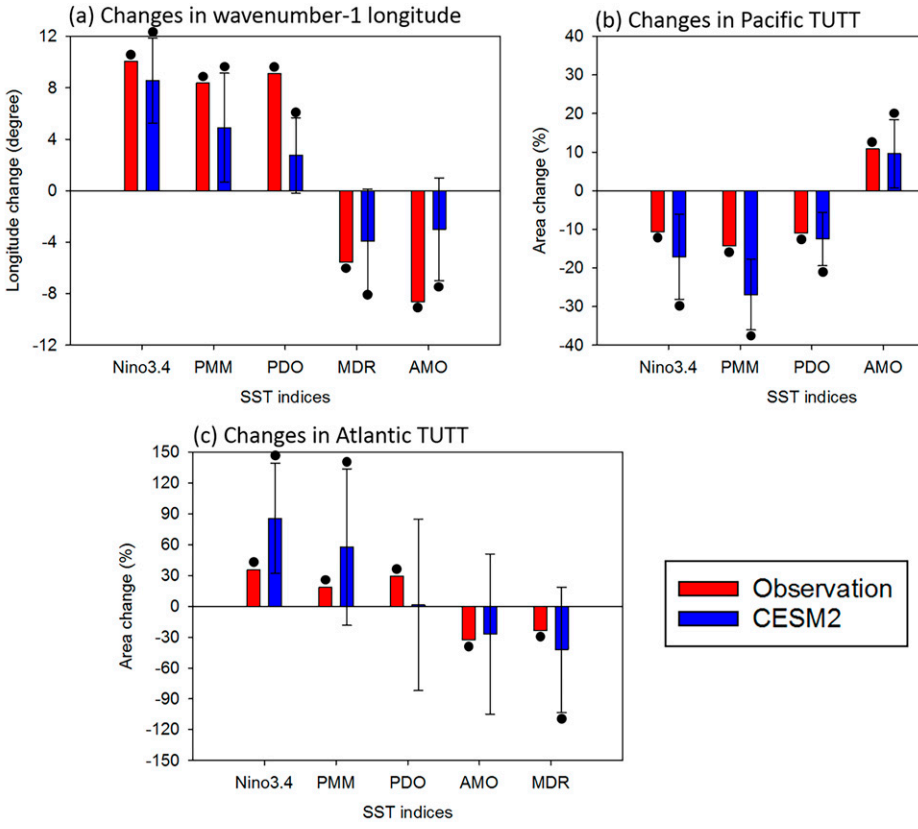

FIG. 8. (a) Observed WN1's longitude (°) change corresponding to +1 STD of various SST indices (red bars), and ensemble-mean responses of WN1's longitude (°) to different SST forcings (blue bars). Whiskers are standard deviations between 20 members, and black dots denote the regression or ensemble-mean difference is significant at 95% confidence level. (b) As in (a), but for change in Pacific TUTT area (%). (c) As in (a), but for change in Atlantic TUTT area (%).

directly comparable to Figs. 5c and 5f, as the latter only represent the ENSO impacts via the variability of WN1 longitude.

Patterns of heating anomalies associated with the PMM and PDO have some similarities, as the heating increases in both experiments over the equatorial and tropical North Pacific, but the latter has a weaker magnitude than the former (Figs. 7c,d). The 200-hPa Psi* response shows an anomalous anticyclonic circulation over the tropical–subtropical central Pacific and an anomalous cyclone over the tropical North Atlantic (Figs. 7b–d), and the magnitude of 200-hPa Psi* anomaly is the weakest in the PDO experiment (Fig. 7d). The anomalous upper-level anticyclones show a similar structure in all three experiments and can be regarded as a Gill-Matsuno-type response (Gill 1980) to tropical diabatic heating, which has been linked to the above-normal tropical Pacific SST by previous studies (Hu and Feng 2012; Li et al. 2015; Liu et al. 2021).

The positive phase of AMO and the warming in the tropical North Atlantic both excite an anomalous anticyclone extending from the Gulf of Mexico to the eastern Pacific (Figs. 7e,f), which is associated with enhanced heating over the tropical North Atlantic and Central America (Kushnir et al. 2010). Meanwhile, both experiments show weak but significant negative heating anomalies over the off-equatorial region of central North Pacific (Figs. 7e,f), consistent with the weakened Pacific ITCZ observed during the warm phase of AMM (e.g., Ham et al. 2013). Similarities between the AMO and MDR experiments over the Western Hemisphere suggest that AMO influences subtropical stationary waves mainly through its tropical branch, consistent with previous studies suggesting that most of the climate impacts from AMO are driven by tropical SST anomalies (Davini et al. 2015; Ruprich-Robert et al. 2017; Sutton 2005; Sutton and Hodson 2007).

Now we focus on changes in the WN1 longitude and TUTTs in our experiments and compare them with the observation (Fig. 8). Despite some magnitude differences from the observation, CESM2 qualitatively reproduces the observed responses of WN1 longitude, Pacific TUTT, and Atlantic TUTT to the different SST forcings. Both observation and simulations indicate that the WN1 shifts eastward, the Pacific TUTT weakens, and the Atlantic TUTT strengthens in response to the El Niño–like warming, or the positive phases of PMM and PDO (Fig. 8). In contrast to the Pacific SST forcing, opposite changes in WN1's longitude and TUTTs can result from anomalously warm SST over the tropical Atlantic or the positive phase of the AMO.

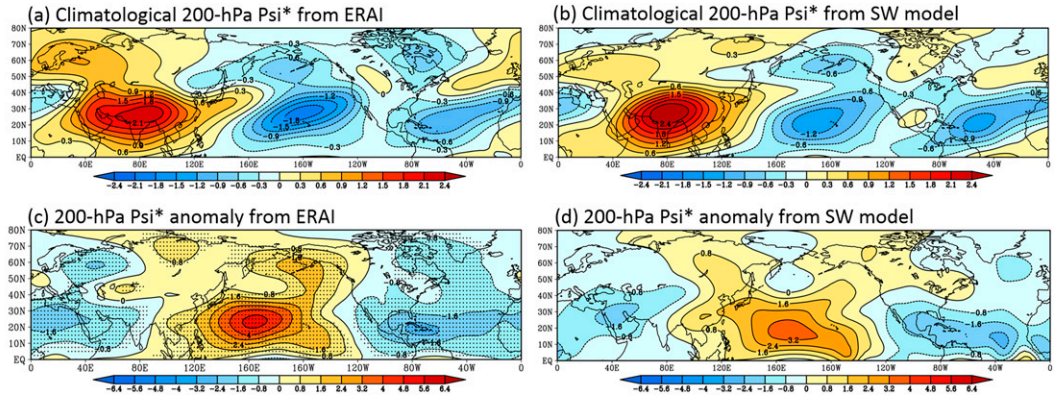

FIG. 9. (a) Climatological 200-hPa Psi* (10^7 m^2 s^{-1}) from ERAI. (b) Response of 200-hPa Psi* (10^7 m^2 s^{-1}) in the SWM when it is forced by observed orography, climatological diabatic heating, and transient momentum forcing. (c) Observed 200-hPa Psi* (10^6 m^2 s^{-1}) change corresponding to +1 STD of WN1's longitude. (d) Response of 200-hPa Psi* (10^6 m^2 s^{-1}) when the SWM is subjected to simultaneous changes in basic states, diabatic heating, and transient forcing corresponding to +1 STD of WN1's longitude.

We primarily focus here on the linear climate responses to different SST forcings by investigating the differences between the SST+ and SST− experiments. However, the Northern Hemispheric climate does not vary in a fully linear manner with respect to different phases of ENSO and AMO (Hoerling et al. 1997; Sung et al. 2015). We thus further examined the differences between individual groups of experiments, SST+ and SST−, and the CTRL. The 200-hPa Psi* responses are nearly opposite between the warm and cool phases, but positive SST forcing induces a larger longitudinal shift of WN1 (not shown).

c. *Insights from a simple stationary wave model*

The CESM2 simulations help us confirm the causal relation and isolate the impacts of individual SST modes. The control of SST forcing on stationary wave variability may largely reside in its capability to modulate precipitation and latent heating (Lindzen and Nigam 1987; Neelin and Held 1987), but extratropical disturbances sometimes intrude equatorward and significantly affect the tropical convective activity (Kiladis 1998; Waugh and Polvani 2000; Waugh 2005). Therefore, reconciling the tropical and extratropical controls is important for understanding the variability of stationary waves. In this section, the linear stationary wave model (SWM) is used to further investigate the basic drivers of anomalous stationary waves. The relative impacts of tropical and extratropical processes on subtropical stationary wave variability will be assessed as well.

1) BASIC DRIVERS OF STATIONARY WAVE VARIABILITY

Before examining the dynamical mechanisms involved in maintaining the anomalous stationary waves, we first compute the response of SWM to total forcing derived from ERAI (Fig. 9b), which includes orography, long-term mean global diabatic heating, and transient momentum fluxes. The SWM faithfully reproduces the observed climatological stationary wave pattern (Figs. 9a,b), as indicated by the high pattern correlation coefficient ($r = 0.94$) of 200-hPa Psi* between the ERAI (Fig. 9a) and the response in SWM (Fig. 9b) over 0°–45°N. Some discrepancies still exist. For example, the Pacific TUTT is too weak, and the Asian monsoon anticyclone and Atlantic TUTT simulated by SWM are slightly stronger than these observed in ERAI (Figs. 9a,b).

Variations of basic states, transient forcing, and diabatic heating are calculated with respect to +1 STD of WN1's longitude (Figs. 10b,f,h). When the SWM is subjected to simultaneous changes in basic states, transient eddies, and diabatic heating, it can reproduce the robust features of the observed anomalous stationary waves, characterized by the strengthened anticyclonic circulation straddling the central North Pacific, and an elongated band of negative Psi* anomaly extending from Mexico to the Arabian Sea (Figs. 9c,d). Nevertheless, there are a few discrepancies between Figs. 9c and 9d. The anomalous anticyclone over the North Pacific is about 30% weaker compared with the observations, and the observed wave train pattern north of 50°N (Fig. 9c) is poorly represented in the SWM (Fig. 9d). A plausible explanation is that zonal-mean flows, transient eddies, and diabatic heating are coupled together and interact with each other in nature, but such interaction is not included in the SWM. The idealized 15-day damping that is applied to the SWM could be another reason responsible for the weaker-than-observed Psi* response. Despite the differences, the simulated wave responses and the observations overall show a better agreement in the subtropics. It is thus possible to decompose the effect of each forcing mechanism and investigate their relative importance.

In Fig. 10, the linear model response shown in Fig. 9d is decomposed into three components: the response to change in basic states (Fig. 10e), transient eddies (Fig. 10g), and diabatic heating (Fig. 10a). The similarity between Figs. 9d and 10a indicates that diabatic heating is the primary driver for the interannual variability of subtropical stationary waves. Interestingly, even though the influence of ENSO is removed from the

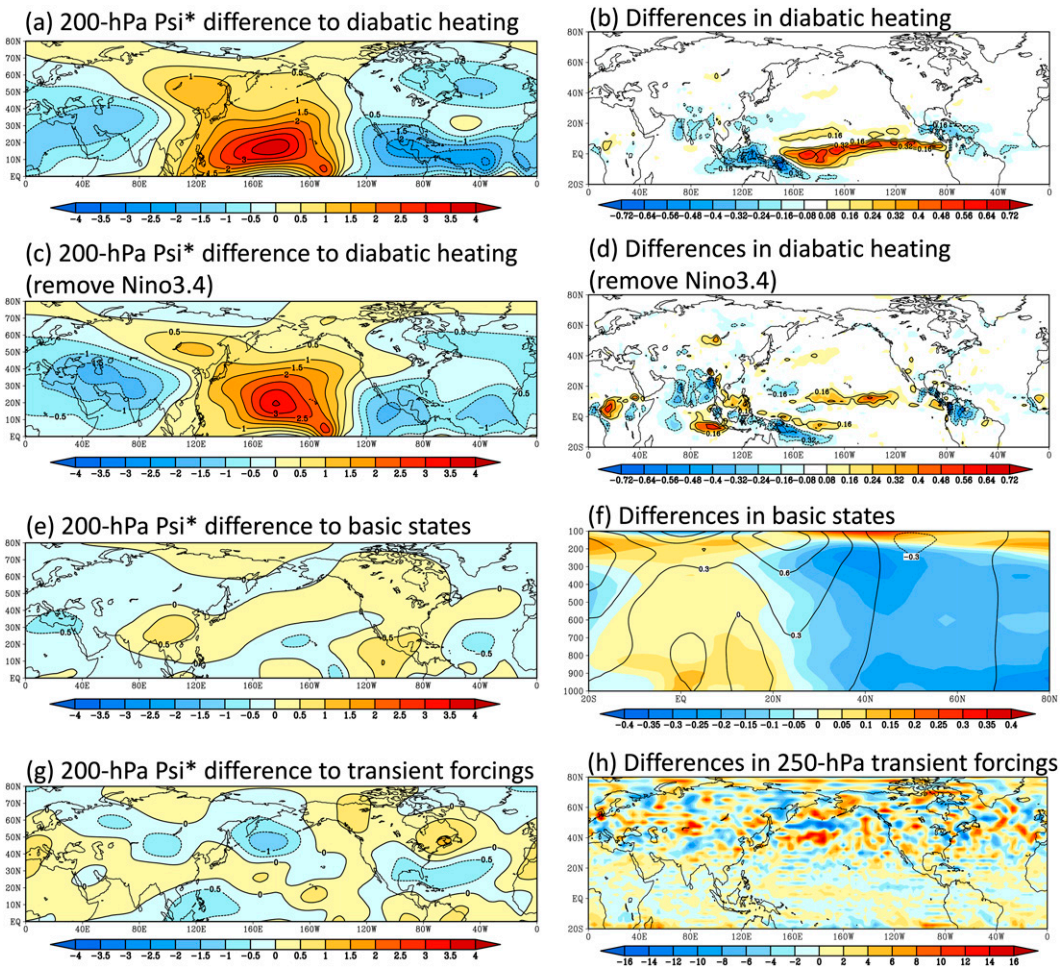

FIG. 10. (a) Responses of 200-hPa Psi* (10^6 m^2 s^{-1}) in the SWM forced by (b) changes in diabatic heating. (c),(d) As in (a) and (b), but heating anomalies related to ENSO are removed using least squares linear regression. (e) Responses of 200-hPa Psi* (10^6 m^2 s^{-1}) forced by (f) anomalous basic states. In (f), contours are anomalous zonal-mean zonal wind (m s^{-1}), and shaded parts represent anomalous zonal-mean temperature (K). (g) Responses of 200-hPa Psi* (10^6 m^2 s^{-1}) induced by (h) anomalous transient momentum fluxes (10^{-10} s^{-2}). The changes in basic states in (b), diabatic heating in (f), and transient forcings in (h) are calculated with respect to +1 STD of WN1's longitude.

diabatic forcing (Fig. 10d), the linear model response to the residual heating (Fig. 10c) reproduces most of the subtropical stationary wave pattern forced by total diabatic forcing (Fig. 10a) although with a reduced magnitude. As explained by Sardeshmukh and Hoskins (1988), the ENSO-related equatorial heating anomalies are not a very effective Rossby wave source, compared to the tropical heating near the subtropical westerly jets where the background vorticity gradient is large. Therefore, ENSO is just one of the important drivers for the variability of subtropical stationary waves (Figs. 10a,c).

Transient eddies play a more important role than changes in basic states (Figs. 10e,g) and make a comparable contribution to diabatic heating in shaping the zonal asymmetries north of 45°N (Figs. 10a,g). They act to weaken the Pacific TUTT but strengthen the Atlantic TUTT (Fig. 10g) and contribute to an out-of-phase relation between the subtropical North Pacific and subtropical North Atlantic. We also notice that transient eddy forcing generates a wave train pattern spanning from the tropical western Pacific to the subtropical North Atlantic (Fig. 10g). The wave train pattern bears resemblance to a weather regime that favors anticyclonic RWB over the subtropical Atlantic (see Fig. 8a in Zhang and Wang 2019). Frequent occurrences of RWB can help maintain or intensify TUTT on the seasonal time scale through its interaction with the background mean flow (Horinouchi et al. 2000; Postel and Hitchman 1999).

2) TROPICAL VERSUS EXTRATROPICAL PROCESSES

The control of tropical SST forcing on TUTTs has been suggested by several studies (Deng et al. 2018; Lu et al. 2017; Wang and Wu 2016; Wang et al. 2020), while extratropical RWB was also acknowledged as an important contributor in maintaining the strength of upper troughs through transporting PV from the stratospheric reservoir equatorward into

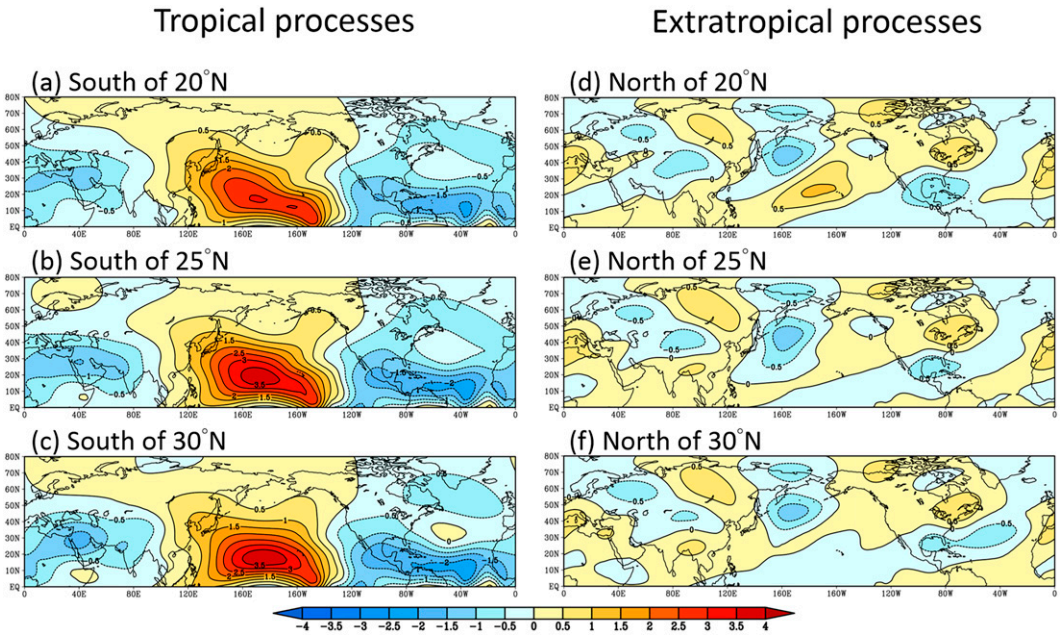

FIG. 11. Responses of 200-hPa Psi* to changes in diabatic heating and transient forcing south of (a) 20°N, (b) 25°N, and (c) 30°N, individually. (d)–(f) As in (a)–(c), but north of 20°, 25°, and 30°N, respectively. In the experiments focusing on the tropical processes [i.e., (a)–(c)], variations in transient forcing and diabatic heating are set to zeros north of different dividing latitudes, whereas these are prescribed as zeros south of the dividing latitudes in the extratropical processes simulations [i.e., (d)–(f)].

subtropical latitudes (Postel and Hitchman 1999). In addition to TUTTs, the anticyclone above Tibet is traditionally regarded as a direct response to the heat source over the Indian and western Pacific monsoon regions (Hoskins and Rodwell 1995; Ting 1994), but recent studies based on observations and idealized experiments (Mölg et al. 2017; Rupp and Haynes 2021) suggested that the Asian monsoon anticyclone interacts actively with the midlatitude jet and baroclinic eddies. These studies suggested that we need to look beyond the tropics to better understand the variability of subtropical stationary waves.

The relative contribution of tropical and extratropical processes to the eastward shift of WN1 is investigated by prescribing anomalies in diabatic heating and transient momentum fluxes over the tropics or extratropics. Three dividing latitudes are tested: 20°, 25°, and 30°N (Fig. 11). The spatial patterns of the responses are largely insensitive to these dividing latitudes. Tropical forcing (Figs. 11a–c), particularly diabatic heating (Fig. 10a), contributes most to the phase shift of WN1, and the magnitude of 200-hPa Psi* response becomes stronger when the dividing latitude shifts poleward (Figs. 11a,b). When forced by the extratropical processes (Figs. 11d–f), the spatial structure of 200-hPa Psi* response north of 40°N reproduces key features of Fig. 10g and presents a zonal wavenumber-3 pattern. Over the subtropics, the extratropical forcing helps extend the circulation of Atlantic TUTT westward to the Gulf of Mexico and sets up a distinct dipole flow configuration over the Tibetan Plateau, which acts to shift the center of Asian monsoon anticyclone southward (Figs. 11d–f). Overall, the simulations suggest that tropical diabatic heating plays the primary role in modulating subtropical stationary waves while the impacts of transient momentum fluxes are weaker but not negligible.

5. Discussion and conclusions

Subtropical stationary waves play a leading role in shaping hydrological heterogeneity across different regions in the world (Chen and Bordoni 2014; Ferreira et al. 2018; Molnar et al. 2010; Rodwell and Hoskins 1996; Simpson et al. 2015; Wills and Schneider 2015). Recently, occurrences of extreme weathers, such as heat waves, droughts, and extreme precipitation, have been linked to anomalous planetary waves (e.g., Coumou et al. 2014; Ma and Franzke 2021; Petoukhov et al. 2013; Yuan et al. 2015). This study examines the interannual variability of summertime subtropical stationary waves and their connections to regional TC activity, a subject of less focus. The forcing mechanisms for stationary wave variability are also explored using the CESM2 and a baroclinic stationary wave model.

Observational evidence shows that the variability of the subtropical stationary waves can be largely explained by the longitudinal displacement of the zonal wavenumber-1 component and the intensity change of the zonal wavenumber-2 component. These two indices are strongly anticorrelated and offer simple metrics to characterize the variability of stationary waves. An eastward shift of the wavenumber-one component occurs in concert with significantly weakened wavenumber-2 intensity. At the same time, Pacific TUTT weakens whereas

the Atlantic TUTT intensifies. Variations of TUTT extent are accompanied by significant changes in large-scale environmental conditions and basinwide TC activity. The tropical North Atlantic is subjected to stronger VWS and reduced tropospheric precipitable water. Additionally, frequent anticyclonic RWB occurrence not only facilitates exchange of momentum and mass (e.g., moisture and ozone) between extratropics and tropics but also help to maintain the strength of Atlantic TUTT through the eddy–mean flow interaction (Horinouchi et al. 2000; Postel and Hitchman 1999). These factors constitute unfavorable conditions for TC genesis and intensification over the tropical North Atlantic. In contrast, increased TC activity over the EPAC and the eastern portion of WNP is associated with weakened TUTT and reduced occurrences of RWB over the central Pacific. Opposite large-scale circulation anomalies and responses of regional TC activity are observed when the WN1 component displaces westward. Multidecadal long-term trends show a coherent story: the position of WN1 has displaced westward, and the strength of WN2 has intensified, consistent with the strengthened Pacific TUTT but weakened Atlantic TUTT from 1979 to 2018 (Fig. S3; also see Wang et al. 2020). Variations of TUTTs may help explain the westward shift of the tropical cyclogenesis locations over the WNP (Wu et al. 2015) and the enhanced North Atlantic TC activity (e.g., Balaguru et al. 2018; Zhao et al. 2018) in recent decades.

Statistical analyses indicate a strong linkage of WN1's longitude change to different air–sea coupled climate modes. Various SST perturbation experiments using CESM2 are performed to explore the causality and disentangle the roles of different large-scale SST modes. Results suggest that the longitude of the wavenumber-1 component and TUTTs are strongly affected by the ENSO, PMM, and the tropical North Atlantic SST anomalies. Further diagnosis using a baroclinic stationary wave model delineates the dominant role of tropical diabatic heating in driving the interannual variability of stationary waves in the subtropics. Impacts of different air–sea coupled modes on subtropical stationary waves can be understood primarily by their influences on tropical large-scale convective overturning motion and associated precipitation (Lindzen and Nigam 1987; Neelin and Held 1987). From a dynamical perspective, upper-level divergence due to tropical convective activity serves as an effective Rossby wave source (Sardeshmukh and Hoskins 1988) as the divergent flow redistributes vorticity through vortex stretching and advection. On the other hand, transient eddies play a nonnegligible role in modulating the strength of TUTTs, possibly through RWB. Finally, it is worth noting that the observational analysis and model simulations convey the same message: ENSO is just one of the important drivers for the variability of subtropical stationary waves, and ENSO alone does not provide a complete picture to understand the stationary wave–TC relationship.

The actual role played by upper-level transients in modulating stationary waves might be greater than that diagnosed by the simple SWM. First, diabatic heating in the tropics can be strongly affected by extratropical disturbance, such as RWB, from the synoptic to intraseasonal time scales (Funatsu and Waugh 2008; Kiladis 1998; Tomaziello et al. 2016; Vigaud and Robertson 2017). At the leading edge of the intruding PV tongue, reduced static stability and enhanced upward motion initiate and support deep convection (Funatsu and Waugh 2008); in contrast, tropical convection is substantially suppressed within the high-PV tongue owing to the equatorward transport of extratropical dry air from the lowermost stratosphere (Waugh 2005; Zhang et al. 2017). Additionally, extratropical weather perturbations influence the evolution of SST through modulations of turbulent and radiative fluxes (Strong and Magnusdottir 2008; Zhang and Wang 2019). Although tropical forcing can be regarded as the primary driver for subtropical stationary wave variability, extratropical processes may play a more important role in modulating regional TC activity and tropospheric circulations than the local SST in certain years (Chang and Wang 2018). A better understanding of both tropical and extratropical variability will help improve the predictions of regional TC activity (Zhang and Wang 2019) and subtropical stationary waves.

Although influences of subtropical stationary waves on regional TC activity can be partly attributed to variations in TUTT extents and the associated changes in environmental conditions, other forcing mechanisms could also be important. For example, the strong impacts of regional Hadley circulation and Walker circulation on TC activity over the North Atlantic and EPAC have been emphasized by previous studies (e.g., Molinari and Vollaro 2017; Patricola et al. 2017; Zhang and Wang 2013, 2015), and TC genesis location and typhoon number over the WNP are found to have a close relationship with the Walker circulation and monsoon trough (Chan 1985; Ritchie and Holland 1999; Song et al. 2020). These large-scale circulations are strongly coupled with variations in tropospheric heating, and their impacts are implicitly represented by the anomalous subtropical stationary waves. On the other hand, subtropical stationary waves should not be regarded as a "root driver" for TC variability. Instead, they serve as a unified framework to understand the impacts of various forcing agents, such as ENSO, AMM, and extratropical RWB, on TC activity over the North Atlantic and North Pacific. The framework provides new insight into the connections between atmospheric general circulation and regional TC variability with a more complete physical picture accounting for the recently established RWB–TC relationship from the intraseasonal-to-seasonal time scales (Li et al. 2018; Papin et al. 2020; Zhang et al. 2016, 2017). A better understanding of the response in stationary waves and TUTTs to global warming will increase our confidence in projecting the future changes of regional TC activity, and this will be reported in a future study. Finally, the potential connection between subtropical stationary waves and TC variability in the Southern Hemisphere will be another interesting direction to explore for future studies.

Acknowledgments. This work was supported by the NOAA MAPP NA16OAR4310080/NSF grant ATM-2116804 and was based on chapter 4 of Chuan-Chieh Chang's Ph.D. thesis (Chang 2021) at the University of Illinois at Urbana-Champaign. We thank Dr. Pu Lin and Dr. Kun Gao for helpful comments on the initial draft of the manuscript. High-performance

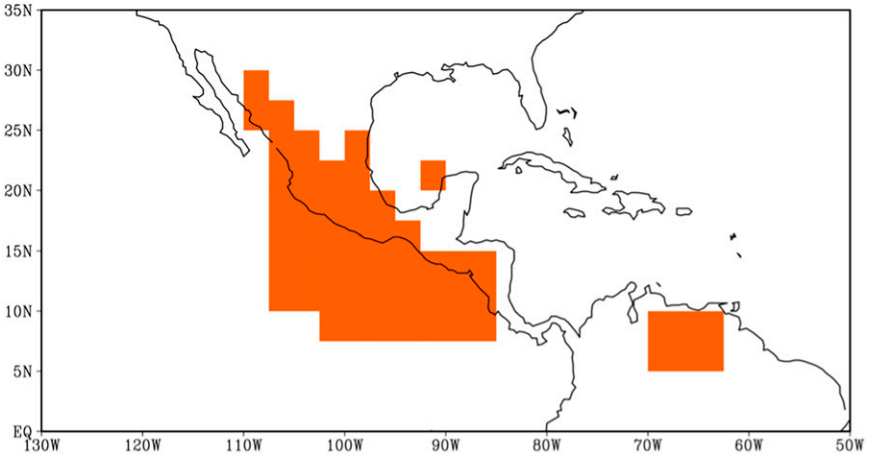

FIG. C1. Domain for the Central American monsoon.

computing resources for CESM2 simulations are provided by the Texas Advanced Computing Center (TACC) at the University of Texas at Austin, and the Blue Waters supercomputer at National Center for Supercomputing Applications (NCSA) at the University of Illinois at Urbana-Champaign.

Data availability statement. The ERAI reanalysis data are available through the NCAR Research Data Archive (RDA) (https://rda.ucar.edu/datasets/ds627.0/). The PMM index was calculated by Prof. Daniel Vimont at University of Wisconsin–Madison (https://www.aos.wisc.edu/~dvimont/MModes/Data.html) and the PDO index is listed on https://www.ncdc.noaa.gov/teleconnections/pdo/. HURDAT2 was provided by Atlantic Oceanographic and Meteorological Laboratory (AOML)/NOAA Hurricane Research Division (https://www.nhc.noaa.gov/data/#hurdat). Best-track data from JTWC are from https://www.metoc.navy.mil/jtwc/jtwc.html?best-tracks, GPCP precipitation is available from https://psl.noaa.gov/data/gridded/data.gpcp.html, and ERSSTv5 data are available from https://psl.noaa.gov/data/gridded/data.noaa.ersst.v5.html.

APPENDIX A

Definitions of Different Climate Indices

1) MDR SST is the SST averaged over the Atlantic main development region (10°–20°N, 20°–80°W).
2) Niño-3.4 SST is the SST averaged over the Niño-3.4 region (5°S–5°N, 120°–170°W).
3) The AMO index is calculated using the method described in Trenberth and Shea (2006). First, the JASO SST anomalies averaged over the North Atlantic (0°–60°N, 0°–80°W), relative to the long-term mean during 1979–2018, are calculated, and the SST anomalies over the global oceans (60°S–60°N, 0°–360°) are obtained using the same approach. Then the AMO index is defined as the difference of SST anomalies between the North Atlantic and the global oceans (North Atlantic minus global oceans).
4) The PDO index is obtained from the NOAA National Centers for Environmental Information website: https://www.ncdc.noaa.gov/teleconnections/pdo/#mantua-1999.
5) The PMM index is provided by http://www.aos.wisc.edu/~dvimont/MModes/Data.html, which is maintained by Dr. Dan Vimont.

APPENDIX B

Equations of Different Forcing Terms

Diabatic heating (Q1), transient vorticity forcing (TF_v), and transient divergence forcing (TF_D) are calculated using the following equations:

$$Q1 = \frac{T}{\theta}\left(\frac{\partial\theta}{\partial t} + u\frac{\partial\theta}{\partial x} + v\frac{\partial\theta}{\partial y} + \omega\frac{\partial\theta}{\partial p}\right), \tag{B1}$$

$$TF_v = -\frac{\partial\overline{\zeta' u'}}{\partial x} - \frac{\partial\overline{\zeta' v'}}{\partial y} - \left[\frac{\partial}{\partial x}\left(\overline{\omega'\frac{\partial v'}{\partial p}}\right) - \frac{\partial}{\partial y}\left(\overline{\omega'\frac{\partial u'}{\partial p}}\right)\right], \tag{B2}$$

$$TF_D = \frac{\partial\overline{\zeta' v'}}{\partial x} - \frac{\partial\overline{\zeta' u'}}{\partial y} - \frac{\partial}{\partial x}\left(\overline{\omega'\frac{\partial u'}{\partial p}}\right) - \frac{\partial}{\partial y}\left(\overline{\omega'\frac{\partial v'}{\partial p}}\right) - \frac{\partial^2}{\partial x^2}\left[\frac{1}{2}(\overline{u'^2} + \overline{v'^2})\right] - \frac{\partial^2}{\partial y^2}\left[\frac{1}{2}(\overline{u'^2} + \overline{v'^2})\right], \tag{B3}$$

where u, v, ω, ζ, T, θ, and p are the three-dimensional wind components, relative vorticity, temperature, potential temperature, and pressure. The climatological state is denoted by an overbar, and deviation from the mean is represented by a prime.

APPENDIX C

Definitions of Different Monsoon Indices

1) The South Asia monsoon index is based on the magnitude of the mean zonal wind shear between 850 and 200 hPa

($U_{850} - U_{200}$) over the South Asia region (40°–110°E, 0°–20°N; Webster and Yang 1992).

2) The western North Pacific monsoon is defined as the difference of 850-hPa westerlies between a southern region (5°–15°N, 100°–130°E) and a northern region (20°–30°N, 110°–140°E; Wang et al. 2001).
3) Following Akinsanola and Zhou (2020), the West African summer monsoon index (WASMI) is defined as:

$$\text{WASMI} = 0.08U_{850} + 0.1U_{700} - 0.04U_{150} + 6.2,$$

where U_{850} is the zonal wind at the 850-hPa level, U_{700} is the zonal wind at 700 hPa, and U_{150} is the zonal wind at 150 hPa averaged between latitude 4° and 10°N and longitude 20°W and 20°E.

1) Xu and Guan (2017) calculated the outgoing longwave anomaly over the Maritime Continent region (10°S–10°N, 95°–145°E) as an approximation for the convective strength of the Maritime Continent monsoon. Here the Maritime Continent monsoon index is defined as the averaged seasonal precipitation over the same region (10°S–10°N, 95°–145°E).
2) The Central America monsoon index is defined as the seasonal-mean precipitation over the monsoon domain. Following Wang and Ding (2008), the monsoon precipitation domain (Fig. C1) over Central America is defined by the region where the monsoon precipitation index (MPI) is greater than 0.5 and the annual range of precipitation is greater than 300 mm. Here the MPI is defined as

$$\text{MPI} = \frac{\text{annual range of precipitation}}{\text{annual mean precipitation}}.$$

The annual range can be defined by the local summer (May–September) minus winter (November–March) precipitation over the Northern Hemisphere.

REFERENCES

Adams, D. K., and A. C. Comrie, 1997: The North American monsoon. *Bull. Amer. Meteor. Soc.*, **78**, 2197–2214, https://doi.org/10.1175/1520-0477(1997)078<2197:TNAM>2.0.CO;2.

Adler, R. F., and Coauthors, 2003: The version-2 Global Precipitation Climatology Project (GPCP) monthly precipitation analysis (1979–present). *J. Hydrometeor.*, **4**, 1147–1167, https://doi.org/10.1175/1525-7541(2003)004<1147:TVGPCP>2.0.CO;2.

Akinsanola, A. A., and W. Zhou, 2020: Understanding the variability of West African summer monsoon rainfall: Contrasting tropospheric features and monsoon index. *Atmosphere*, **11**, 309, https://doi.org/10.3390/atmos11030309.

Alexander, M. A., D. J. Vimont, P. Chang, and J. D. Scott, 2010: The impact of extratropical atmospheric variability on ENSO: Testing the seasonal footprinting mechanism using coupled model experiments. *J. Climate*, **23**, 2885–2901, https://doi.org/10.1175/2010JCLI3205.1.

Balaguru, K., G. R. Foltz, and L. R. Leung, 2018: Increasing magnitude of hurricane rapid intensification in the central and eastern tropical Atlantic. *Geophys. Res. Lett.*, **45**, 4238–4247, https://doi.org/10.1029/2018GL077597.

Bell, G. D., and Coauthors, 2000: Climate assessment for 1999. *Bull. Amer. Meteor. Soc.*, **81** (6), S1–S50, https://doi.org/10.1175/1520-0477(2000)81[s1:CAF]2.0.CO;2.

Bhardwaj, P., D. R. Pattanaik, and O. Singh, 2019: Tropical cyclone activity over Bay of Bengal in relation to El Niño–Southern Oscillation. *Int. J. Climatol.*, **39**, 5452–5469, https://doi.org/10.1002/joc.6165.

Camargo, S. J., and A. H. Sobel, 2005: Western North Pacific tropical cyclone intensity and ENSO. *J. Climate*, **18**, 2996–3006, https://doi.org/10.1175/JCLI3457.1.

——, K. A. Emanuel, and A. H. Sobel, 2007: Use of a genesis potential index to diagnose ENSO effects on tropical cyclone genesis. *J. Climate*, **20**, 4819–4834, https://doi.org/10.1175/JCLI4282.1.

Camp, J., and Coauthors, 2019: The western Pacific subtropical high and tropical cyclone landfall: Seasonal forecasts using the Met Office GloSea5 system. *Quart. J. Roy. Meteor. Soc.*, **145**, 105–116, https://doi.org/10.1002/qj.3407.

Cassou, C., C. Deser, L. Terray, J. W. Hurrell, and M. Drévillon, 2004: Summer sea surface temperature conditions in the North Atlantic and their impact upon the atmospheric circulation in early winter. *J. Climate*, **17**, 3349–3363, https://doi.org/10.1175/1520-0442(2004)017<3349:SSSTCI>2.0.CO;2.

Chan, J. C. L., 1985: Tropical cyclone activity in the northwest Pacific in relation to the El Niño/Southern Oscillation phenomenon. *Mon. Wea. Rev.*, **113**, 599–606, https://doi.org/10.1175/1520-0493(1985)113<0599:TCAITN>2.0.CO;2.

Chang, C.-C., 2021: Extratropical impacts on variability and prediction of tropical cyclone activity. Ph.D. dissertation, University of Illinois at Urbana-Champaign, 279 pp.

——, and Z. Wang, 2018: Relative impacts of local and remote forcing on tropical cyclone frequency in numerical model simulations. *Geophys. Res. Lett.*, **45**, 7843–7850, https://doi.org/10.1029/2018GL078606.

Chang, C.-P., Y. Zhang, and T. Li, 2000: Interannual and interdecadal variations of the East Asian summer monsoon and tropical Pacific SSTs. Part I: Roles of the subtropical ridge. *J. Climate*, **13**, 4310–4325, https://doi.org/10.1175/1520-0442(2000)013<4310:IAIVOT>2.0.CO;2.

Chen, J., and S. Bordoni, 2014: Orographic effects of the Tibetan Plateau on the East Asian summer monsoon: An energetic perspective. *J. Climate*, **27**, 3052–3072, https://doi.org/10.1175/JCLI-D-13-00479.1.

Chen, S., and K. E. Trenberth, 1988: Forced planetary waves in the Northern Hemisphere winter: Wave-coupled orographic and thermal forcings. *J. Atmos. Sci.*, **45**, 682–704, https://doi.org/10.1175/1520-0469(1988)045<0682:FPWITN>2.0.CO;2.

Chen, T., 2003: Maintenance of summer monsoon circulations: A planetary-scale perspective. *J. Climate*, **16**, 2022–2037, https://doi.org/10.1175/1520-0442(2003)016<2022:MOSMCA>2.0.CO;2.

——, 2005: The structure and maintenance of stationary waves in the winter Northern Hemisphere. *J. Atmos. Sci.*, **62**, 3637–3660, https://doi.org/10.1175/JAS3566.1.

Chiang, J. C., and D. J. Vimont, 2004: Analogous Pacific and Atlantic meridional modes of tropical atmosphere–ocean variability. *J. Climate*, **17**, 4143–4158, https://doi.org/10.1175/JCLI4953.1.

Coumou, D., V. Petoukhov, S. Rahmstorf, S. Petri, and H. J. Schellnhuber, 2014: Quasi-resonant circulation regimes and hemispheric synchronization of extreme weather in boreal summer. *Proc. Natl. Acad. Sci. USA*, **111**, 12 331–12 336, https://doi.org/10.1073/pnas.1412797111.

Czaja, A., and J. Marshall, 2001: Observations of atmosphere–ocean coupling in the North Atlantic. *Quart. J. Roy. Meteor. Soc.*, **127**, 1893–1916, https://doi.org/10.1002/qj.49712757603.

——, and C. Frankignoul, 2002: Observed impact of Atlantic SST anomalies on the North Atlantic Oscillation. *J. Climate*, **15**, 606–623, https://doi.org/10.1175/1520-0442(2002)015<0606:OIOASA>2.0.CO;2.

Dai, A., and T. M. L. Wigley, 2000: Global patterns of ENSO-induced precipitation. *Geophys. Res. Lett.*, **27**, 1283–1286, https://doi.org/10.1029/1999GL011140.

Danabasoglu, G., and Coauthors, 2020: The Community Earth System Model version 2 (CESM2). *J. Adv. Model. Earth Syst.*, **12**, e2019MS001916, https://doi.org/10.1029/2019MS001916.

Davini, P., J. Von Hardenberg, and S. Corti, 2015: Tropical origin for the impacts of the Atlantic multidecadal variability on the Euro-Atlantic climate. *Environ. Res. Lett.*, **10**, 094010, https://doi.org/10.1088/1748-9326/10/9/094010.

Dee, D. P., and Coauthors, 2011: The ERA-Interim reanalysis: Configuration and performance of the data assimilation system. *Quart. J. Roy. Meteor. Soc.*, **137**, 553–597, https://doi.org/10.1002/qj.828.

Deng, K., S. Yang, M. Ting, C. Hu, and M. Lu, 2018: Variations of the mid-Pacific trough and their relations to the Asian–Pacific–North American climate: Roles of tropical sea surface temperature and Arctic sea ice. *J. Climate*, **31**, 2233–2252, https://doi.org/10.1175/JCLI-D-17-0064.1.

Elsner, J. B., and A. B. Kara, 1999: *Hurricanes of the North Atlantic: Climate and Society*. Oxford University Press, 488 pp.

Enfield, D. B., A. M. Mestas-Nuñez, and P. J. Trimble, 2001: The Atlantic multidecadal oscillation and its relation to rainfall and river flows in the continental U.S. *Geophys. Res. Lett.*, **28**, 2077–2080, https://doi.org/10.1029/2000GL012745.

Ferreira, D., and Coauthors, 2018: Atlantic–Pacific asymmetry in deep water formation. *Annu. Rev. Earth Planet. Sci.*, **46**, 327–352, https://doi.org/10.1146/annurev-earth-082517-010045.

Fitzpatrick, P. J., J. A. Knaff, C. W. Landsea, and S. V. Finley, 1995: Documentation of a systematic bias in the aviation model's forecast of the Atlantic tropical upper-tropospheric trough: Implications for tropical cyclone forecasting. *Wea. Forecasting*, **10**, 433–446, https://doi.org/10.1175/1520-0434(1995)010<0433:DOASBI>2.0.CO;2.

Funatsu, B. M., and D. W. Waugh, 2008: Connections between potential vorticity intrusions and convection in the eastern tropical Pacific. *J. Atmos. Sci.*, **65**, 987–1002, https://doi.org/10.1175/2007JAS2248.1.

Geller, M. A., and S. K. Avery, 1978: Northern Hemisphere distributions of diabatic heating in the troposphere derived from general circulation data. *Mon. Wea. Rev.*, **106**, 629–636, https://doi.org/10.1175/1520-0493(1978)106<0629:NHDODH>2.0.CO;2.

Gill, A. E., 1980: Some simple solutions for heat-induced tropical circulation. *Quart. J. Roy. Meteor. Soc.*, **106**, 447–462, https://doi.org/10.1002/qj.49710644905.

Gray, W. M., 1984: Atlantic seasonal hurricane frequency. Part I: El Niño and 30 mb quasi-biennial oscillation influences. *Mon. Wea. Rev.*, **112**, 1649–1668, https://doi.org/10.1175/1520-0493(1984)112<1649:ASHFPI>2.0.CO;2.

Ham, Y. G., and Coauthors, 2013: Sea surface temperature in the north tropical Atlantic as a trigger for El Niño/Southern Oscillation events. *Nat. Geosci.*, **6**, 112–116, https://doi.org/10.1038/ngeo1686.

Held, I. M., M. Ting, and H. Wang, 2002: Northern winter stationary waves: Theory and modeling. *J. Climate*, **15**, 2125–2144, https://doi.org/10.1175/1520-0442(2002)015<2125:NWSWTA>2.0.CO;2.

Hoerling, M. P., A. Kumar, and M. Zhong, 1997: El Niño, La Niña, and the nonlinearity of their teleconnections. *J. Climate*, **10**, 1769–1786, https://doi.org/10.1175/1520-0442(1997)010<1769:ENOLNA>2.0.CO;2.

Horinouchi, T., F. Sassi, and B. A. Boville, 2000: Synoptic-scale Rossby waves and the geographic distribution of lateral transport routes between the tropics and the extratropics in the lower stratosphere. *J. Geophys. Res.*, **105**, 26 579–26 592, https://doi.org/10.1029/2000JD900281.

Hoskins, B. J., and M. J. Rodwell, 1995: A model of the Asian summer monsoon. Part I: The global scale. *J. Atmos. Sci.*, **52**, 1329–1340, https://doi.org/10.1175/1520-0469(1995)052<1329:AMOTAS>2.0.CO;2.

Hu, Q., and S. Feng, 2012: AMO- and ENSO-driven summertime circulation and precipitation variations in North America. *J. Climate*, **25**, 6477–6495, https://doi.org/10.1175/JCLI-D-11-00520.1.

Huang, B., and Coauthors, 2017: Extended Reconstructed Sea Surface Temperature, version 5 (ERSSTv5): Upgrades, validations, and intercomparisons. *J. Climate*, **30**, 8179–8205, https://doi.org/10.1175/JCLI-D-16-0836.1.

Johnson, R. H., 2003: Thermal low. *Encyclopedia of Atmospheric Sciences*, Academic Press, 2269–2273.

Joly, M., and A. Voldoire, 2009: Influence of ENSO on the West African monsoon: Temporal aspects and atmospheric processes. *J. Climate*, **22**, 3193–3210, https://doi.org/10.1175/2008JCLI2450.1.

Jong, B., M. Ting, R. Seager, and W. B. Anderson, 2020: ENSO teleconnections and impacts on U.S. summertime temperature during a multiyear La Niña life cycle. *J. Climate*, **33**, 6009–6024, https://doi.org/10.1175/JCLI-D-19-0701.1.

Kiladis, G. N., 1998: Observations of Rossby waves linked to convection over the eastern tropical Pacific. *J. Atmos. Sci.*, **55**, 321–339, https://doi.org/10.1175/1520-0469(1998)055<0321:OORWLT>2.0.CO;2.

Knaff, J. A., 1997: Implications of summertime sea level pressure anomalies in the tropical Atlantic region. *J. Climate*, **10**, 789–804, https://doi.org/10.1175/1520-0442(1997)010<0789:IOSSLP>2.0.CO;2.

Krishnamurti, T. N., 1971: Observational study of the tropical upper tropospheric motion field during the Northern Hemisphere summer. *J. Appl. Meteor. Climatol.*, **10**, 1066–1096, https://doi.org/10.1175/1520-0450(1971)010<1066:OSOTTU>2.0.CO;2.

Kushnir, Y., R. Seager, M. Ting, N. Naik, and J. Nakamura, 2010: Mechanisms of tropical Atlantic SST influence on North American precipitation variability. *J. Climate*, **23**, 5610–5628, https://doi.org/10.1175/2010JCLI3172.1.

Landsea, C. W., and J. L. Franklin, 2013: Atlantic hurricane database uncertainty and presentation of a new database format. *Mon. Wea. Rev.*, **141**, 3576–3592, https://doi.org/10.1175/MWR-D-12-00254.1.

Lawrence, D. M., and Coauthors, 2019: The Community Land Model version 5: Description of new features, benchmarking, and impact of forcing uncertainty. *J. Adv. Model. Earth Syst.*, **11**, 4245–4287, https://doi.org/10.1029/2018MS001583.

Lenggenhager, S., 2013: Tropical cyclone tracks and the subtropical high pressure system in the North-Atlantic in a 400-year climate simulation. M.S. thesis, Faculty of Science, University of Bern, 67 pp.

Li, W., L. Li, R. Fu, Y. Deng, and H. Wang, 2011: Changes to the North Atlantic subtropical high and its role in the intensification of summer rainfall variability in the southeastern United States. *J. Climate*, **24**, 1499–1506, https://doi.org/10.1175/2010JCLI3829.1.

——, ——, and Y. Deng, 2015: Impact of the interdecadal Pacific oscillation on tropical cyclone activity in the North Atlantic and eastern North Pacific. *Sci. Rep.*, **5**, 12358, https://doi.org/10.1038/srep12358.

——, Z. Wang, G. Zhang, M. S. Peng, S. G. Benjamin, and M. Zhao, 2018: Subseasonal variability of Rossby wave breaking and impacts on tropical cyclones during the North Atlantic warm season. *J. Climate*, **31**, 9679–9695, https://doi.org/10.1175/JCLI-D-17-0880.1.

Li, X., S.-P. Xie, S. T. Gille, and C. Yoo, 2016: Atlantic-induced pan-tropical climate change over the past three decades. *Nat. Climate Change*, **6**, 275–279, https://doi.org/10.1038/nclimate2840.

Lindzen, R. S., and S. Nigam, 1987: On the role of sea surface temperature gradients in forcing low-level winds and convergence in the tropics. *J. Atmos. Sci.*, **44**, 2418–2436, https://doi.org/10.1175/1520-0469(1987)044<2418:OTROSS>2.0.CO;2.

Ling, J., and C. Zhang, 2013: Diabatic heating profiles in recent global reanalyses. *J. Climate*, **26**, 3307–3325, https://doi.org/10.1175/JCLI-D-12-00384.1.

Liu, A. Z., M. Ting, and H. Wang, 1998: Maintenance of circulation anomalies during the 1988 drought and 1993 floods over the United States. *J. Atmos. Sci.*, **55**, 2810–2832, https://doi.org/10.1175/1520-0469(1998)055<2810:MOCADT>2.0.CO;2.

Liu, Z., T. Gao, W. Zhang, and M. Luo, 2021: Implications of the Pacific meridional mode for summer precipitation extremes over China. *Wea. Climate Extremes*, **33**, 100359, https://doi.org/10.1016/j.wace.2021.100359.

Lu, M., K. Deng, S. Yang, G. Zhou, and Y. Tan, 2017: Interannual and interdecadal variations of the mid-Atlantic trough and associated American–Atlantic–Eurasian climate anomalies. *Atmos.–Ocean*, **55**, 284–292, https://doi.org/10.1080/07055900.2017.1369931.

Ma, Q., and C. L. E. Franzke, 2021: The role of transient eddies and diabatic heating in the maintenance of European heat waves: A nonlinear quasi-stationary wave perspective. *Climate Dyn.*, **56**, 2983–3002, https://doi.org/10.1007/s00382-021-05628-9.

Magaña, V., and M. Yanai, 1991: Tropical–midlatitude interaction on the time scale of 30 to 60 days during the northern summer of 1979. *J. Climate*, **4**, 180–201, https://doi.org/10.1175/1520-0442(1991)004<0180:TMIOTT>2.0.CO;2.

Mantua, N. J., S. R. Hare, Y. Zhang, J. M. Wallace, and R. C. Francis, 1997: A Pacific interdecadal climate oscillation with impacts on salmon production. *Bull. Amer. Meteor. Soc.*, **78**, 1069–1079, https://doi.org/10.1175/1520-0477(1997)078<1069:APICOW>2.0.CO;2.

Mei, W., S. Xie, and M. Zhao, 2014: Variability of tropical cyclone track density in the North Atlantic: Observations and high-resolution simulations. *J. Climate*, **27**, 4797–4814, https://doi.org/10.1175/JCLI-D-13-00587.1.

Mo, K. C., J. Nogues-Paegle, and J. Paegle, 1995: Physical mechanisms of the 1993 summer floods. *J. Atmos. Sci.*, **52**, 879–895, https://doi.org/10.1175/1520-0469(1995)052<0879:PMOTSF>2.0.CO;2.

Mölg, T., F. Maussion, E. Collier, J. Chiang, and D. Scherer, 2017: Prominent midlatitude circulation signature in High Asia's surface climate during monsoon: Circulation influences on High Asia. *J. Geophys. Res. Atmos.*, **122**, 12 702–12 712, https://doi.org/10.1002/2017JD027414.

Molinari, J., and D. Vollaro, 2017: Monsoon gyres of the northwest Pacific: Influences of ENSO, the MJO, and the Pacific–Japan pattern. *J. Climate*, **30**, 1765–1777, https://doi.org/10.1175/JCLI-D-16-0393.1.

Molnar, P., W. R. Boos, and D. S. Battisti, 2010: Orographic controls on climate and paleoclimate of Asia: Thermal and mechanical roles for the Tibetan Plateau. *Annu. Rev. Earth Planet. Sci.*, **38**, 77–102, https://doi.org/10.1146/annurev-earth-040809-152456.

Neelin, J. D., and I. M. Held, 1987: Modeling tropical convergence based on the moist static energy budget. *Mon. Wea. Rev.*, **115**, 3–12, https://doi.org/10.1175/1520-0493(1987)115<0003:MTCBOT>2.0.CO;2.

Nigam, S., and E. DeWeaver, 2003: Stationary waves (orographically and thermally forced). *Encyclopedia of Atmospheric Sciences*, J. R. Holton et al., Eds., Academic Press, 2121–2137.

Nobre, P., and J. Shukla, 1996: Variations of sea surface temperature, wind stress, and rainfall over the tropical Atlantic and South America. *J. Climate*, **9**, 2464–2479, https://doi.org/10.1175/1520-0442(1996)009<2464:VOSSTW>2.0.CO;2.

Ortega, S., P. J. Webster, V. Toma, and H.-R. Chang, 2018: The effect of potential vorticity fluxes on the circulation of the tropical upper troposphere. *Quart. J. Roy. Meteor. Soc.*, **144**, 848–860, https://doi.org/10.1002/qj.3261.

Papin, P. P., L. F. Bosart, and R. D. Torn, 2020: A feature-based approach to classifying summertime potential vorticity streamers linked to Rossby wave breaking in the North Atlantic Basin. *J. Climate*, **33**, 5953–5969, https://doi.org/10.1175/JCLI-D-19-0812.1.

Patricola, C. M., R. Saravanan, and P. Chang, 2017: A teleconnection between Atlantic sea surface temperature and eastern and central North Pacific tropical cyclones. *Geophys. Res. Lett.*, **44**, 1167–1174, https://doi.org/10.1002/2016GL071965.

Petoukhov, V., S. Rahmstorf, S. Petri, and H. J. Schellnhuber, 2013: Quasiresonant amplification of planetary waves and recent Northern Hemisphere weather extremes. *Proc. Natl. Acad. Sci. USA*, **110**, 5336–5341, https://doi.org/10.1073/pnas.1222000110.

Postel, G. A., and M. H. Hitchman, 1999: A climatology of Rossby wave breaking along the subtropical tropopause. *J. Atmos. Sci.*, **56**, 359–373, https://doi.org/10.1175/1520-0469(1999)056<0359:ACORWB>2.0.CO;2.

Rayner, N. A., 2003: Global analyses of sea surface temperature, sea ice, and night marine air temperature since the late nineteenth century. *J. Geophys. Res.*, **108**, 4407–4436, https://doi.org/10.1029/2002JD002670.

Ritchie, E. A., and G. J. Holland, 1999: Large-scale patterns associated with tropical cyclogenesis in the western Pacific. *Mon. Wea. Rev.*, **127**, 2027–2043, https://doi.org/10.1175/1520-0493(1999)127<2027:LSPAWT>2.0.CO;2.

Rodwell, M. J., and B. J. Hoskins, 1996: Monsoons and the dynamics of deserts. *Quart. J. Roy. Meteor. Soc.*, **122**, 1385–1404, https://doi.org/10.1002/qj.49712253408.

Rupp, P., and P. Haynes, 2021: Zonal scale and temporal variability of the Asian monsoon anticyclone in an idealised numerical model. *Wea. Climate Dyn.*, **2**, 413–431, https://doi.org/10.5194/wcd-2-413-2021.

Ruprich-Robert, Y., R. Msadek, F. Castruccio, S. Yeager, T. Delworth, and G. Danabasoglu, 2017: Assessing the climate impacts of the observed Atlantic multidecadal variability using the GFDL CM2.1 and NCAR CESM1 global coupled

models. *J. Climate*, **30**, 2785–2810, https://doi.org/10.1175/JCLI-D-16-0127.1.

Sadler, J. C., 1967: The tropical upper tropospheric trough as a secondary source of typhoons and a primary source of trade wind disturbances. Hawaii Institute of Geophysics, University of Hawaii Tech. Rep. 67-12, 44 pp.

Sardeshmukh, P. D., and B. J. Hoskins, 1988: The generation of global rotational flow by steady idealized tropical divergence. *J. Atmos. Sci.*, **45**, 1228–1251, https://doi.org/10.1175/1520-0469(1988)045<1228:TGOGRF>2.0.CO;2.

Schubert, S., H. Wang, and M. Suarez, 2011: Warm season subseasonal variability and climate extremes in the Northern Hemisphere: The role of stationary Rossby waves. *J. Climate*, **24**, 4773–4792, https://doi.org/10.1175/JCLI-D-10-05035.1.

Simpson, I. R., R. Seager, T. A. Shaw, and M. Ting, 2015: Mediterranean summer climate and the importance of Middle East topography. *J. Climate*, **28**, 1977–1996, https://doi.org/10.1175/JCLI-D-14-00298.1.

——, ——, M. Ting, and T. A. Shaw, 2016: Causes of change in Northern Hemisphere winter meridional winds and regional hydroclimate. *Nat. Climate Change*, **6**, 65–70, https://doi.org/10.1038/nclimate2783.

——, and Coauthors, 2020: An evaluation of the large-scale atmospheric circulation and its variability in CESM2 and other CMIP models. *J. Geophys. Res. Atmos.*, **125**, e2020JD032835, https://doi.org/10.1029/2020JD032835.

Siu, L. W., and K. P. Bowman, 2019: Forcing of the upper-tropospheric monsoon anticyclones. *J. Atmos. Sci.*, **76**, 1937–1954, https://doi.org/10.1175/JAS-D-18-0340.1.

Smith, A. B., and R. W. Katz, 2013: US billion-dollar weather and climate disasters: Data sources, trends, accuracy and biases. *Nat. Hazards*, **67**, 387–410, https://doi.org/10.1007/s11069-013-0566-5.

Song, J., P. J. Klotzbach, and Y. Duan, 2020: Differences in western North Pacific tropical cyclone activity among three El Niño phases. *J. Climate*, **33**, 7983–8002, https://doi.org/10.1175/JCLI-D-20-0162.1.

Strong, C., and G. Magnusdottir, 2008: Tropospheric Rossby wave breaking and the NAO/NAM. *J. Atmos. Sci.*, **65**, 2861–2876, https://doi.org/10.1175/2008JAS2632.1.

Sung, M.-K., S.-I. An, B.-M. Kim, and J.-S. Kug, 2015: Asymmetric impact of Atlantic Multidecadal Oscillation on El Niño and La Niña characteristics. *Geophys. Res. Lett.*, **42**, 4998–5004, https://doi.org/10.1002/2015GL064381.

Sutton, R. T., 2005: Atlantic Ocean forcing of North American and European summer climate. *Science*, **309**, 115–118, https://doi.org/10.1126/science.1109496.

——, and D. L. R. Hodson, 2007: Climate response to basin-scale warming and cooling of the North Atlantic Ocean. *J. Climate*, **20**, 891–907, https://doi.org/10.1175/JCLI4038.1.

Teng, H., and Coauthors, 2013: Probability of US heat waves affected by a subseasonal planetary wave pattern. *Nat. Geosci.*, **6**, 1056–1061, https://doi.org/10.1038/ngeo1988.

——, G. Branstator, G. A. Meehl, and W. M. Washington, 2016: Projected intensification of subseasonal temperature variability and heat waves in the Great Plains. *Geophys. Res. Lett.*, **43**, 2165–2173, https://doi.org/10.1002/2015GL067574.

Ting, M., 1994: Maintenance of northern summer stationary waves in a GCM. *J. Atmos. Sci.*, **51**, 3286–3308, https://doi.org/10.1175/1520-0469(1994)051<3286:MONSSW>2.0.CO;2.

——, and L. Yu, 1998: Steady response to tropical heating in wavy linear and nonlinear baroclinic models. *J. Atmos. Sci.*, **55**, 3565–3582, https://doi.org/10.1175/1520-0469(1998)055<3565:SRTTHI>2.0.CO;2.

——, H. Wang, and L. Yu, 2001: Nonlinear stationary wave maintenance and seasonal cycle in the GFDL R30 GCM. *J. Atmos. Sci.*, **58**, 2331–2354, https://doi.org/10.1175/1520-0469(2001)058<2331:NSWMAS>2.0.CO;2.

Tomaziello, A. C. N., L. M. V. Carvalho, and A. W. Gandu, 2016: Intraseasonal variability of the Atlantic intertropical convergence zone during austral summer and winter. *Climate Dyn.*, **47**, 1717–1733, https://doi.org/10.1007/s00382-015-2929-y.

Trenberth, K. E., and C. J. Guillemot, 1996: Physical processes involved in the 1988 drought and 1993 floods in North America. *J. Climate*, **9**, 1288–1298, https://doi.org/10.1175/1520-0442(1996)009<1288:PPIITD>2.0.CO;2.

——, and D. J. Shea, 2006: Atlantic hurricanes and natural variability in 2005. *Geophys. Res. Lett.*, **33**, L12704, https://doi.org/10.1029/2006GL026894.

Vigaud, N., and A. Robertson, 2017: Convection regimes and tropical–midlatitude interactions over the Intra-American Seas from May to November. *Int. J. Climatol.*, **37**, 987–1000, https://doi.org/10.1002/joc.5051.

Wallace, J. M., and P. V. Hobbs, 1977: *Atmospheric Science: An Introductory Survey*. Academic Press, 467 pp.

Wang, B., and Q. H. Ding, 2008: Global monsoon: Dominant mode of annual variation in the tropics. *Dyn. Atmos. Oceans*, **44**, 165–183, https://doi.org/10.1016/j.dynatmoce.2007.05.002.

——, R. Wu, and K.-M. Lau, 2001: Interannual variability of the Asian summer monsoon: Contrasts between the Indian and the western North Pacific–East Asian monsoons. *J. Climate*, **14**, 4073–4090, https://doi.org/10.1175/1520-0442(2001)014<4073:IVOTAS>2.0.CO;2.

Wang, C., and L. Wu, 2016: Interannual shift of the tropical upper-tropospheric trough and its influence on tropical cyclone formation over the western North Pacific. *J. Climate*, **29**, 4203–4211, https://doi.org/10.1175/JCLI-D-15-0653.1.

——, and Coauthors, 2013: Seasonal modulations of different impacts of two types of ENSO events on tropical cyclone activity in the western North Pacific. *Climate Dyn.*, **40**, 2887–2902, https://doi.org/10.1007/s00382-012-1434-9.

Wang, Z., G. Zhang, T. J. Dunkerton, and F.-F. Jin, 2020: Summertime stationary waves integrate tropical and extratropical impacts on tropical cyclone activity. *Proc. Natl. Acad. Sci. USA*, **117**, 22 720–22 726, https://doi.org/10.1073/pnas.2010547117.

Waugh, D. W., 2005: Impact of potential vorticity intrusions on subtropical upper tropospheric humidity. *J. Geophys. Res.*, **110**, D11305, https://doi.org/10.1029/2004JD005664.

——, and L. M. Polvani, 2000: Climatology of intrusions into the tropical upper troposphere. *Geophys. Res. Lett.*, **27**, 3857–3860, https://doi.org/10.1029/2000GL012250.

Webster, P. J., and S. Yang, 1992: Monsoon and ENSO: Selectively interactive systems. *Quart. J. Roy. Meteor. Soc.*, **118**, 877–926, https://doi.org/10.1002/qj.49711850705.

White, G. H., 1982: An observational study of the Northern Hemisphere extratropical summer general circulation. *J. Atmos. Sci.*, **39**, 24–40, https://doi.org/10.1175/1520-0469(1982)039<0024:AOSOTN>2.0.CO;2.

White, R. H., K. Kornhuber, O. Martius, and V. Wirth, 2022: From atmospheric waves to heatwaves: A waveguide perspective for understanding and predicting concurrent, persistent, and extreme extratropical weather. *Bull. Amer. Meteor. Soc.*, **103**, E923–E935, https://doi.org/10.1175/BAMS-D-21-0170.1.

Wills, R. C., and T. Schneider, 2015: Stationary eddies and the zonal asymmetry of net precipitation and ocean freshwater forcing. *J. Climate*, **28**, 5115–5133, https://doi.org/10.1175/JCLI-D-14-00573.1.

——, R. H. White, and X. J. Levine, 2019: Northern Hemisphere stationary waves in a changing climate. *Curr. Climate Change Rep.*, **5**, 372–389, https://doi.org/10.1007/s40641-019-00147-6.

Wolf, G., D. J. Brayshaw, N. P. Klingaman, and A. Czaja, 2018: Quasi-stationary waves and their impact on European weather and extreme events. *Quart. J. Roy. Meteor. Soc.*, **144**, 2431–2448, https://doi.org/10.1002/qj.3310.

Wu, G., and N.-C. Lau, 1992: A GCM simulation of the relationship between tropical-storm formation and ENSO. *Mon. Wea. Rev.*, **120**, 958–977, https://doi.org/10.1175/1520-0493(1992)120<0958:AGSOTR>2.0.CO;2.

Wu, L., C. Wang, and B. Wang, 2015: Westward shift of western North Pacific tropical cyclogenesis. *Geophys. Res. Lett.*, **42**, 1537–1542, https://doi.org/10.1002/2015GL063450.

Wu, Q., X. Wang, and L. Tao, 2020: Interannual and interdecadal impact of western North Pacific subtropical high on tropical cyclone activity. *Climate Dyn.*, **54**, 2237–2248, https://doi.org/10.1007/s00382-019-05110-7.

Xu, Q., and Z. Guan, 2017: Interannual variability of summertime outgoing longwave radiation over the Maritime Continent in relation to East Asian summer monsoon anomalies. *J. Meteor. Res.*, **31**, 665–677, https://doi.org/10.1007/s13351-017-6178-3.

Yuan, J., W. Li, and Y. Deng, 2015: Amplified subtropical stationary waves in boreal summer and their implications for regional water extremes. *Environ. Res. Lett.*, **10**, 104009, https://doi.org/10.1088/1748-9326/10/10/104009.

Zhang, G., and Z. Wang, 2013: Interannual variability of the Atlantic Hadley circulation in boreal summer and its impacts on tropical cyclone activity. *J. Climate*, **26**, 8529–8544, https://doi.org/10.1175/JCLI-D-12-00802.1.

——, and ——, 2015: Interannual variability of tropical cyclone activity and regional Hadley circulation over the northeastern Pacific. *Geophys. Res. Lett.*, **42**, 2473–2481, https://doi.org/10.1002/2015GL063318.

——, and ——, 2018: North Atlantic extratropical Rossby wave breaking during the warm season: Wave life cycle and role of diabatic heating. *Mon. Wea. Rev.*, **146**, 695–712, https://doi.org/10.1175/MWR-D-17-0204.1.

——, and ——, 2019: North Atlantic Rossby wave breaking during the hurricane season: Association with tropical and extratropical variability. *J. Climate*, **32**, 3777–3801, https://doi.org/10.1175/JCLI-D-18-0299.1.

——, ——, T. J. Dunkerton, M. S. Peng, and G. Magnusdottir, 2016: Extratropical impacts on Atlantic tropical cyclone activity. *J. Atmos. Sci.*, **73**, 1401–1418, https://doi.org/10.1175/JAS-D-15-0154.1.

——, ——, M. S. Peng, and G. Magnusdottir, 2017: Characteristics and impacts of extratropical Rossby wave breaking during the Atlantic hurricane season. *J. Climate*, **30**, 2363–2379, https://doi.org/10.1175/JCLI-D-16-0425.1.

Zhang, Y., J. M. Wallace, and D. S. Battisti, 1997: ENSO-like interdecadal variability: 1900–93. *J. Climate*, **10**, 1004–1020, https://doi.org/10.1175/1520-0442(1997)010<1004:ELIV>2.0.CO;2.

Zhao, H., X. Duan, G. B. Raga, and F. Sun, 2018: Potential large-scale forcing mechanisms driving enhanced North Atlantic tropical cyclone activity since the mid-1990s. *J. Climate*, **31**, 1377–1397, https://doi.org/10.1175/JCLI-D-17-0016.1.